RSC Advances

PAPER

View Article Online
View Journal | View Issue

Cite this: *RSC Adv.*, 2025, **15**, 6424

Dihydropyrimidine-2-thione derivatives as SARS-CoV-2 main protease inhibitors: synthesis, SAR and *in vitro* profiling†

Anees Saeed, [a] Ayesha Tahir,[a] Muhammad Shah,[a] Fahad Hussain, [a] Abdul Sadiq[b] and Umer Rashid *[a]

Despite the passage of approximately five years since the outbreak, an efficacious remedy for SARS-CoV-2 remains elusive, highlighting the urgent imperative for developing SARS-CoV-2 potent inhibitors. In our current study, we have unmasked the hitherto unrealized potential of dihydropyrimidine-2-thiones against the Main Protease (M^{pro}) of SARS-CoV-2. Employing a predictive docking tool, we identified promising lead compounds and optimized them *via* comprehensive Structural Activity Relationship (SAR) studies. Key design elements included proton donor/acceptor groups, six-membered rings, and fluorinated moieties to enhance interactions. These leads underwent *in vitro* inhibition assays to enhance their interaction with key M^{pro} amino acid residues. Our findings indicated that all synthesized compounds exhibited significant inhibition of the M^{pro}. Compounds **12j** (IC_{50} = 0.063 μM), and **12l** (IC_{50} = 0.054 μM) displayed exceptional *in vitro* binding affinities. In addition to their string inhibitory activity, CC_{50} values were assessed, confirming acceptable cytotoxicity profiles for potent compounds. Molecular dynamic simulation substantiated the binding mechanism revealing that compound **12l** maintains robust stability with the target protein. Furthermore, compounds predicted to have minimal oral toxicity and high intestinal absorption make them promising candidates for drug development. These findings paved the way for the potent clinical application of these dihydropyrimidine-2-thiones as efficient SARS-CoV-2 therapeutics.

Received 29th November 2024
Accepted 19th February 2025

DOI: 10.1039/d4ra08449g

rsc.li/rsc-advances

Introduction

COVID-19 is caused by a deadly Severe Acute Respiratory Syndrome Coronavirus-2 (SARS-CoV-2) that targets the human respiratory system. Coronaviruses such as NL63, OC43, 229E, and HKU1, have generally caused mild respiratory infections like the common cold in humans.[1–5] However, highly pathogenic strains like SARS-CoV-1 (2003), MERS-CoV (2012), and SARS-CoV-2 (2019) have emerged in the past 20 years, posing severe threats to public health. The first SARS-CoV-2 outbreak, reported in Wuhan, China, in 2019, signified the beginning of a global pandemic. SARS-CoV-2, a positive-sense, single-stranded RNA virus within the mammalian beta-coronavirus genus causes respiratory and lung damage leading to potentially fatal illnesses.[6] On March 11, 2020, the World Health Organization (WHO) declared COVID-19, a global pandemic, due to the rapid spread of the virus and the rising mortality rate.[7,8] As of November 25, 2024, WHO reported 776.41 million confirmed cases, 7.075 million deaths, and over 13.64 billion vaccinations globally. Notably, SARS-CoV-2 is among the most infectious virus in the coronavirus family impacting both human and animal populations.[8,9]

SARS-CoV-2 encodes 16 non-structural proteins (NSPs), key structural proteins, membrane (M), nucleocapsid (N), and spike (S) and a Main Protease (M^{pro}) or 3C-like protease ($3CL^{pro}$), Papain Like Protease (PL^{pro}), and RNA-dependent RNA polymerase (RdRp).[10–13] The viral genome, approximately 30 000 nucleotides long, contains a 5′-cap structure, a 3′-poly (A) tail, and multiple open reading frames (ORFs). NSPs possess PL^{pro} and M^{pro} which play a crucial role in viral replication. M^{pro}, comprised of three domains (I–III) and a unique Cys–His dyad active site, is highly conserved across coronaviruses, highlighting its potential as a target for antivirals.[10,14–18] With S1, S1′, S2, and S3 forming the active binding pocket for substrate engagement, M^{pro} facilitates viral protein maturation through peptide bond cleavage, a process validated by mixed quantum mechanics/molecular mechanics (QM/MM) simulations.[19,20] Due to its essential function in the viral life cycle and lack of homologs in humans, M^{pro} is an ideal candidate for therapeutic intervention and drug design.[21–23] Fig. 1 illustrates the M^{pro}'s

[a]*Department of Chemistry, COMSATS University Islamabad, Abbottabad Campus-22060, Pakistan. E-mail: umerrashid@cuiatd.edu.pk*

[b]*Department of Pharmacy, Faculty of Biological Sciences, University of Malakand, Chakdara, 18000 Dir (L), KP, Pakistan*

† Electronic supplementary information (ESI) available. See DOI: https://doi.org/10.1039/d4ra08449g

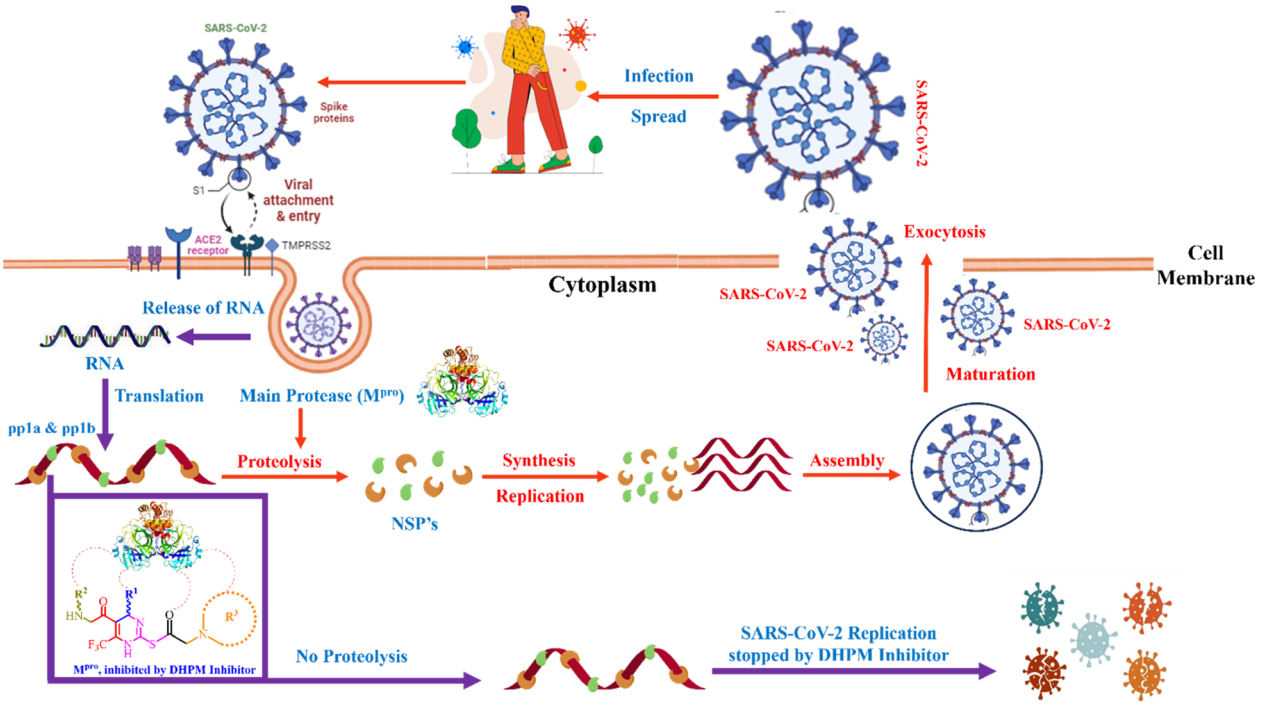

Fig. 1 SARS-CoV-2 M^{pro} inhibition and mechanism of action.

role in viral replication, making protease inhibition a prime target for antiviral drug development.

Currently, FDA-approved COVID-19 inhibitors (Fig. 2) are limited. However, PF-07321332 (nirmatrelvir, $K_i = 0.003$ μM) (**1a**), demonstrates safety, selectivity, and high antiviral activity (EC_{50} of 0.074 μM).[4,24] To counteract its rapid metabolism by CYP3A, the HIV protease inhibitor ritonavir (**1b**) was added, forming Paxlovid, which received FDA approval in 2021 for treating mild to moderate COVID-19. Past studies have identified effective M^{pro} inhibitors, such as PF-00835231 (**1c**) during the SARS-CoV-1 outbreak in 2003.[25] In 2021, Pfizer developed an oral SARS-CoV-2 M^{pro} inhibitor. Japan approved ensitrelvir (S-217622) (**1d**) in 2022, which showed potent M^{pro} inhibition with $IC_{50} = 0.013$ μM and $EC_{50} = 0.37$ μM.[26,27] Several other M^{pro} inhibitors (Fig. 3), including lufotrelvir (**2a**), ebselen (**2b**), and masitinib (**2c**) are in clinical trials while repurposed drugs like boceprevir ($IC_{50} = 4.13$ μM) also exhibit notable inhibitory effects.[28–32]

This work seeks to identify novel dihydropyrimidine-2-thione-based inhibitors with favourable pharmacokinetic properties to combat SARS-CoV-2 effectively by focusing on the design of dihydropyrimidine-2-thione-based derivatives targeting SARS-CoV-2 M^{pro}, aiming to maximize scaffold inhibitory potency. Structure-Based Drug Design (SBDD) techniques were used to optimize and evaluate these scaffolds.[33] The sulphur-rich dihydropyrimidine-2-thione has shown antiviral, antibacterial, and potential anticancer activities. It disrupts viral

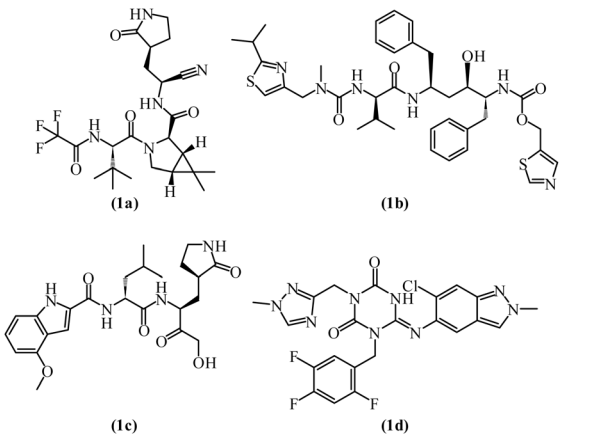

Fig. 2 FDA-approved medication for the treatment of SARS-CoV-2 (**1a–d**).

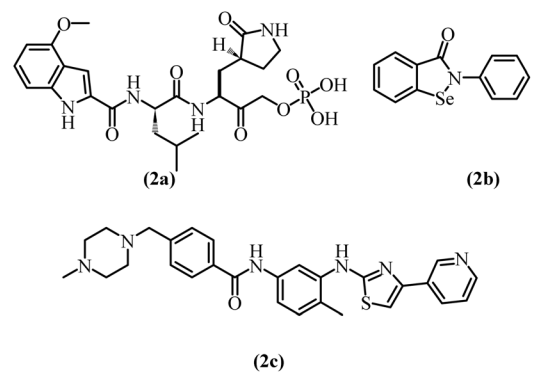

Fig. 3 Medication in clinical trials for the treatment of SARS-CoV-2 (**2a–c**).

replication and hosts immune responses.[34–36] Notably, dihydropyrimidine derivatives such as batzelladine A & B exhibit antiviral properties, while monastrol is known for anticancer activity.[37,38] The antihypertensive drug terazosin exemplified its diverse biological activities.[39]

Materials and methods

General

Solvents and reagents used for current work were purchased from commercial sources and were used without purification. Compounds include substituted aromatic aldehydes (**6a–c**), thiourea, ethyl 4,4,4-trifluoro-3-oxobutanoate, diverse primary amines (L-glutamic acid (**7a**), L-aspartic acid (**7b**), sulfanilic acid (**7c**), L-histidine (**7d**), L-tyrosine (**7e**)), bromoacetyl bromide and diverse secondary amines (**11a–c**) were purchased from Sigma-Aldrich. 400 MHz/100 MHz Bruker NMR spectrometer was used to record ^{1}H and ^{13}C NMR spectra respectively in the DMSO solvent. The solvent was used as an internal reference in NMR analysis. Chemical shifts in NMR analysis are recorded in δ scale part per million (ppm). Thin Layer Chromatography (TLC) was used to monitor the progress of all reactions for current research work on 2 × 5 cm precoated aluminum sheets with silica gel (60-F254), the coating layer thickness specification was 0.25 mm (Merck). Liquid chromatography-mass spectrometry (LC-MS) was performed using Agilent Technologies 1200 series high-performance liquid chromatography system with C18 reversed-phase column (particle size: 3.5 μm, length: 100 mm, internal diameter: 4.6 mm, vendor: Agilent Technologies). Elemental analyses were conducted using an Elemental Vario EI III CHN analyzer. Elemental analysis (±0.4% of the calculated values) was performed for all the tested compounds. Final products were checked for their purity on a HPLC system using a C18 RP column (particle size: 5 μm, length: 150 mm, internal diameter: 4.6 mm, vendor: Shimadzu) and an isocratic solvent system (mentioned in the experimental part) at room temperature. Biologically screened compounds are >95% pure as determined by HPLC.

General method for the synthesis of compounds (6a–c)

Dihydropyrimidine-2-thiones (**6a–c**) core was synthesized by 10 mmol aldehydes (4-(trifluoromethyl)benzaldehyde (**3a**), 4-nitrobenzaldehyde (**3b**) and methyl 4-formyl benzoate (**3c**)) reaction with thiourea (**4**) (10 mmol) and ethyl 4,4,4-trifluoro-3-oxobutanoate (**5**) (12 mmol) through classical multicomponent Biginelli approach using acetonitrile solvent under reflux for 6 h's in the presence of $SnCl_2 \cdot 2H_2O$. Reaction was monitored by TLC, after completion of the reaction the reaction mixture was poured into ice-cold distilled water and allowed to stir for 5 minutes. Precipitates formed, filtered off, dried, washed with cold ethanol, and recrystallized with ethanol to afford pure dihydropyrimidine-2-thiones (**6a–c**).

General method for the synthesis of compounds (8a–h)

Compounds (**8a–h**) are synthesized by the reaction of the substituted dihydropyrimidine-2-thiones (20 mmol, **6a–c**) with diverse primary amines (25 mmol, **7a–e**) in the presence of K_2CO_3 base (1.2 equivalent) in a solvent dimethylformamide (DMF) on heating. The reaction was monitored by TLC, after completion, the reaction mixture was poured into ice water. The precipitates were filtered and washed with cold water and purified with the help of column chromatography (hexane : ethyl acetate 9 : 1 system) to afford pure compounds (**8a–h**). Characterization data of intermediate compounds is presented in the ESI† file.

General method for the synthesis of compounds (10a–h)

To the stirred solution of (5 mmol) synthesized dihydropyrimidine-thione amide derivatives (**8a–h**) in 10 mL acetone solvent, at room temperature, and K_2CO_3 as base and bromoacetyl bromide (**9**) (7.5 mmol) was added dropwise with continuous stirring. The reaction was monitored by TLC and stirring continued for 4 hours. At the end of the reaction precipitated solid was obtained which was further recrystallized by dioxane : ethanol (1 : 1) to furnish *S*-acetylated product/compounds (**10a–h**). Characterization data of intermediate compounds is presented in the ESI† file.

General method for the synthesis of compounds (12a–l)

Diverse secondary amines (5 mmol) (**11a–c**) along with K_2CO_3 base (1.5 eq.) were taken in DMF (10 mL). To this stirred solution previously synthesized *S*-bromoacylated products (**10a–h**) (7.5 mmol) were added. The reaction was monitored by TLC. Stirring continued till the completion of the reaction. Water was added after completion of the reaction to afford precipitation of the products (**12a–l**). In some products, precipitation was not observed. If precipitates were not formed product was not extracted in the organic layer. Later on, all products were purified through column chromatography.

(6-(Trifluoromethyl)-2-((2-(3-(trifluoromethyl)-5,6-dihydro-[1,2,4]triazolo[4,3-*a*]-pyrazin-7(8*H*)-yl)acetyl)thio)-4-(4 (trifluoromethyl)phenyl)-1,4-dihydropyrimidine-5-carbonyl)-L-glutamic acid (12a)

Light yellow solid, yield = 48%, m.p. 199–201 °C; $R_f = 0.47$; (*n*-hexane/EA; 3 : 1); HPLC purity = 97.5% (C18 RP, acetonitrile/H_2O-80 : 20), T_R = 12.1 min. ^{1}H NMR (400 MHz, DMSO-d_6) δ 12.39 (s, 1H, COOH), 11.75 (s, 1H, COOH), 9.38 (s, 1H, py-NH), 8.41 (d, J = 4.72 Hz, –NH), 7.81 (d, J = 8.52 Hz, –2H, ArH), 7.27 (d, J = 8.52 Hz, –2H, ArH), 5.46 (s, 1H, –CH), 4.49–4.45 (m, 1H, glu), 4.26 (t, J = 5.92 Hz, 2H, pip-CH_2), 3.83 (s, 2H, CH_2), 3.28 (s, 2H, pip-CH_2), 3.11 (t, J = 5.92 Hz, 2H, pip-CH_2), 2.27–2.19 (m, 2H, glu), 2.03–1.93 (m, 2H, glu). ^{13}C NMR (100 MHz, DMSO-d_6) δ 190.5, 174.1, 173.6, 162.6, 147.6, 139.7 (q, J = 36.0 Hz, –C–CF_3), 133.8 (q, J = 32.49 Hz, –C–CF_3), 131.7 (q, J = 32.12 Hz, –C–CF_3), 128.1 (2C), 126.9, 125.9, 124.2, 123.4, 122.4, 122.2 (q, J = 269 Hz, –CF_3), 119.9, 116.2, 110.7, 64.8, 59.6, 57.7, 48.4, 41.5, 32.2, 23.4. Analysis calculated for $C_{26}H_{22}F_9N_7O_6S$; C, 42.69; H, 3.03; F, 23.37; N, 13.40; O, 13.12; S, 4.38; found C, 42.56; H, 3.04; N, 13.42; LCMS: m/z = 732.1 $[M + H]^+$.

(6-(Trifluoromethyl)-2-((2-(3-(trifluoromethyl)-5,6-dihydro-[1,2,4]triazolo[4,3-*a*]-pyrazin-7(8*H*)-yl)acetyl)thio)-4-(4-(trifluoromethyl)phenyl)-1,4-dihydropyrimidine-5-carbonyl)-L-aspartic acid (12b)

White solid, yield = 65%, m.p. 204–206 °C; R_f = 0.48; (*n*-hexane/EA; 3 : 1); HPLC purity = 98.6% (C18 RP, acetonitrile/H_2O-80 : 20), T_R = 11.9 min. ^{1}H NMR (400 MHz, DMSO-d_6) δ 12.46 (s, 1H, COOH), 11.81 (s, 1H, COOH), 9.36 (s, 1H, py-NH), 8.40 (d, J = 6.08 Hz, –NH), 7.81 (d, J = 8.36 Hz, –2H, ArH), 7.27 (d, J = 8.36 Hz, –2H, ArH), 5.46 (s, 1H, –CH), 4.44–4.39 (m, 1H, glu), 4.22 (t, J = 5.8 Hz, 2H, pip-CH_2), 3.83 (s, 2H, CH_2), 3.53–3.45 (m, 2H, pip-CH_2), 3.28 (s, 2H, pip-CH_2), 3.10 (t, J = 5.8 Hz, 2H, glu). ^{13}C NMR (100 MHz, DMSO-d_6) δ 188.7, 173.5, 172.9, 164.1, 148.8, 144.9, 142.4, 140.5, 140.2, 132.7, 132.9 (q, J = 36.7 Hz, –C–CF_3), 132.8 (q, J = 32 Hz, –C–CF_3), 131.6 (q, J = 36.5 Hz, –C–CF_3), 127.5, 125.7, 125.2, 124.3, 123.6, 122.4 (q, J = 274 Hz, –CF_3), 117.7, 115.6, 90.7, 61.3, 57.2, 52.8, 50.5, 49.8, 42.7, 36.2. Analysis calculated for $C_{25}H_{20}F_9N_7O_6S$; C, 41.85; H, 2.81; F, 23.83; N, 13.66; O, 13.38; S, 4.47; found C, 41.70; H, 2.82; N, 13.72; LCMS: m/z = 718.1 $[M + H]^+$.

4-(6-(Trifluoromethyl)-2-((2-(3-(trifluoromethyl)-5,6-dihydro[1,2,4]triazolo[4,3-*a*]-pyrazin-7(8*H*)-yl)acetyl)thio)-4-(4-(trifluoromethyl)phenyl)-1,4-dihydropyrimidine-5-carboxamide)benzenesulfonic acid (12c)

Off white solid, yield = 52%, m.p. 182–184 °C; R_f = 0.51; (*n*-hexane/EA; 3 : 1); HPLC purity = 97.3% (C18 RP, acetonitrile/H_2O-80 : 20), T_R = 14.4 min. ^{1}H NMR (400 MHz, DMSO-d_6) δ 10.38 (s, 1H, OH, sulpha), 9.36 (s, 1H, py-NH), 8.69 (s, –NH, sulpha), 7.82 (d, J = 8.32 Hz, –2H, ArH), 7.71 (d, J = 8.56 Hz, –2H, ArH), 7.41 (d, J = 8.56 Hz, –2H, ArH, sulpha), 7.27 (d, J = 8.36 Hz, –2H, ArH), 5.46 (s, 1H, –CH), 4.26 (t, J = 5.84 Hz, 2H, pip-CH_2), 3.83 (s, 2H, CH_2), 3.28 (s, 2H, pip-CH_2), 3.10 (t, J = 5.80 Hz, 2H, pip-CH_2). ^{13}C NMR (100 MHz, DMSO-d_6) δ 188.7, 166.1, 147.5, 144.9, 142.4, 140.7, 139.4, 139.1, 136.3, 133.1, 132.8 (q, J = 36.3 Hz, –C–CF_3), 132.6 (q, J = 32.4 Hz, –C–CF_3), 131.3 (q, J = 36.6 Hz, –C–CF_3), 128.0, 127.5, 125.7, 125.2, 124.7, 123.2, 122.1 (q, J = 271 Hz, –CF_3), 121.3, 119.3, 117.2, 100.1, 61.6, 57.2, 51.2, 50.2, 42.8. Analysis calculated for $C_{27}H_{20}F_9N_7O_5S_2$; C, 42.81; H, 2.66; F, 22.57; N, 12.94; O, 10.56; S, 8.46; found C, 42.94; H, 2.67; F, 22.57; N, 13.00; O, 10.56; S, 8.46; LCMS: m/z = 758.0 $[M + H]^+$.

(6-(Trifluoromethyl)-2-((2-(3-(trifluoromethyl)-5,6-dihydro-[1,2,4]triazolo[4,3-*a*]pyrazin-7(8*H*)-yl)acetyl)thio)-4-(4-(trifluoromethyl)phenyl)-1,4-dihydropyrimidine-5-carbonyl) histidine (12d)

Off white solid, yield = 51%, m.p. 226–228 °C; R_f = 0.45; (*n*-hexane/EA; 3 : 1); HPLC purity = 97.3% (C18 RP, acetonitrile/H2O-80 : 20), TR = 13.7 min. ^{1}H NMR (400 MHz, DMSO-d_6) δ 12.16 (brs, 1H, COOH, His), 9.36 (brs, 1H, py-NH), 8.86 (s, 1H, imidazole, NH), 8.49 (d, J = 6.6 Hz, 1H, CONH, His), 8.03 (s, 1H, imidazole, ArH), 7.82 (d, J = 8.4 Hz, –2H, ArH), 7.26 (d, J = 8.4 Hz, –2H, ArH), 7.07 (s, 1H, imidazole, ArH), 5.46 (s, 1H, –CH), 4.36–4.31 (m, 1H, $CHCH_2$, His), 4.25 (t, J = 576 Hz, 2H, pip-CH_2), 3.83 (s, 2H, CH_2), 3.53–3.45 (m, 2H, $CHCH_2$, His), 3.28 (s, 2H, pip-CH_2), 3.10 (t, J = 5.72 Hz, 2H, pip-CH_2). ^{13}C NMR (100 MHz, DMSO-d_6) δ 188.7, 175.3, 164.5, 148.8, 144.9, 142.4, 140.5, 140.2, 138.8, 135.2, 133.1 (q, J = 36.3 Hz, –C–CF_3), 132.7 (q, J = 36.7 Hz, –C–CF_3), 131.4 (q, J = 36.4 Hz, –C–CF_3), 130.4, 127.5, 125.7, 125.2, 124.9, 123.0, 122.1 (q, J = 272.4 Hz, –CF_3) 118.8, 117.7, 115.6, 90.7, 61.3, 57.2, 54.0, 52.8, 49.8, 42.7, 29.6. Analysis calculated for $C_{27}H_{22}F_9N_9O_4S$; C, 43.85; H, 3.00; F, 23.12; N, 17.05; O, 8.65; S, 4.33; found C, 43.73; H, 3.04; F, 23.12; N, 17.23; O, 8.65; S, 4.33; LCMS: m/z = 740.5 $[M + H]^+$.

(6-(Trifluoromethyl)-2-((2-(3-(trifluoromethyl)-5,6-dihydro-[1,2,4]triazolo[4,3-*a*]-pyrazin-7(8*H*)-yl)acetyl)thio)-4-(4-(trifluoromethyl)phenyl)-1,4-dihydropyrimidine-5-carbonyl)-L-tyrosine (12e)

Cream yellow solid, yield = 54%, m.p. 191–193 °C; R_f = 0.47; (*n*-hexane/EA; 3 : 1); HPLC purity = 97.6% (C18 RP, acetonitrile/H_2O-80 : 20), T_R = 14.3 min. ^{1}H NMR (400 MHz, DMSO-d_6) δ 12.36 (s, 1H, COOH, Tyr), 9.37 (s, 1H, py-NH), 9.08 (s, 1H, Tyr–OH), 8.53 (d, J = 5.28 Hz, 1H, CO–NH), 7.82 (d, J = 8.2 Hz, –2H, ArH), 7.26 (d, J = 8.16 Hz, –2H, ArH), 7.03 (d, J = 7.52 Hz, 2H, Tyr–ArH), 6.76 (d, J = 7.56 Hz, 2H), 5.46 (s, 1H, –CH), 4.98–4.88 (m, 1H, $CHCH_2$ of Tyr), 4.26 (t, J = 5.8 Hz, 2H, pip-CH_2), 3.83 (s, 2H, CH_2), 3.71 (dd, J = 12.44 Hz, J = 9.68 Hz, 1H, CH_2 of Tyr), 3.49 (dd, J = 12.16 Hz, J = 5.16 Hz, 1H, CH_2 of Tyr), 3.28 (s, 2H, pip-CH_2), 3.10 (t, J = 5.8 Hz, 2H, pip-CH_2). ^{13}C NMR (100 MHz, DMSO-d_6) δ 188.4, 177.9, 166.4, 164.5, 157.8, 148.3, 143.8, 141.7, 138.3, 132.3, 131.4, 130.4 (2C), 128.5, 127.6, 125.7 (2C), 125.5 (2C), 124.5, 122.1, 117.3 (2C), 91.5, 61.5, 55.1, 49.3, 48.6, 41.9, 34.1. Analysis calculated for $C_{30}H_{24}F_9N_7O_5S$; C, 47.06; H, 3.16; F, 22.33; N, 12.81; O, 10.45; S, 4.19; found C, 46.88; H, 3.17; F, 22.33; N, 12.85; O, 10.45; S, 4.19; LCMS: m/z = 766.1 $[M + H]^+$.

(2-((2-(3-Aminopiperidin-1-yl)acetyl)thio)-6-(trifluoromethyl)-4-(4-(trifluoromethyl)-phenyl)-1,4-dihydropyrimidine-5-carbonyl)-L-aspartic acid (12f)

Light yellow solid, yield = 61%, m.p. 188–190 °C; R_f = 0.45; (DCM/MeOH; 5 : 1); HPLC purity = 97.8% (C18 RP, acetonitrile/H_2O-80 : 20), T_R = 7.9 min. ^{1}H NMR (400 MHz, $CDCl_3$) δ 12.43 (s, COOH, 1H), 11.80 (s, COOH, 1H), 9.36 (s, py-NH, 1H), 8.40 (d, J = 6.16 Hz, –NH), 7.81 (d, J = 8.4 Hz, 2H, ArH), 7.28 (d, J = 8.4 Hz, 2H, ArH), 5.46 (s, 1H, –CH), 4.44–4.38 (m, 1H, glu), 3.50–3.45 (m, 4H, –CH), 3.31 (s, 2H, CH_2), 3.16–3.12 (m, 1H, CH), 2.67 (d, J = 3.92 Hz, 2H, NH_2), 2.48 (dd, J = 17.28 Hz, J = 5.16 Hz, 6.2 Hz, 1H, CH), 1.60–1.49 (m, 2H, glu), 1.41–1.38 (m, 2H, –CH_2). ^{13}C NMR (100 MHz, $CDCl_3$) δ 188.6, 173.6, 172.4, 166.2, 144.9, 143.1, 132.3, 130.6, 127.5 (2C), 125.3 (2C), 124.3, 123.8, 91.5, 63.1, 59.6, 57.5, 53.6, 49.8, 47.6, 35.8, 34.1, 21.7. Analysis calculated for $C_{24}H_{25}F_6N_5O_6S$; C, 46.08; H, 4.03; F, 18.22; N, 11.20; O, 15.35; S, 5.13; found C, 45.89; H, 4.05; F, 18.22; N, 11.23; O, 15.35; S, 5.13; LCMS: m/z = 626.1 $[M + H]^+$.

(2-((2-(3-Aminopiperidin-1-yl)acetyl)thio)-6-(trifluoromethyl)-4-(4-(trifluoromethyl)-phenyl)-1,4-dihydropyrimidine-5-carbonyl)-L-tyrosine (12g)

Cream yellow solid, yield = 51%, m.p. 199–201 °C; R_f = 0.48; (*n*-hexane/EA; 3 : 1); HPLC purity = 97.6% (C18 RP, acetonitrile/

H_2O-80 : 20), T_R = 13.5 min. ^{1}H NMR (400 MHz, $CDCl_3$) δ 12.36 (s, 1H, COOH, Tyr), 9.36 (s, 1H, py-NH), 9.09 (s, 1H, Tyr–OH), 8.54 (d, J = 5.36 Hz, 1H, CO–NH), 7.81 (d, J = 8.2 Hz, 2H, ArH), 7.28 (d, J = 8.2 Hz, 2H, ArH), 7.03 (d, J = 7.56 Hz, 2H, Tyr–ArH), 6.75 (d, J = 7.56 Hz, 2H, Tyr–ArH), 5.45 (s, 1H, –CH), 4.44–4.38 (m, 1H, $CHCH_2$ of Tyr), 3.30 (s, 2H, CH_2 of Tyr), 3.18–3.14 (m, 3H, –CH), 3.08 (t, J = 5.28 Hz, 2H, CH_2), 2.67 (d, J = 4.4 Hz, 2H, NH_2), 2.47 (dd, J = 17.12 Hz, J = 5.08 Hz, 1H, CH), 1.65–1.50 (m, 2H, –CH_2), 1.44–1.38 (m, 2H, –CH_2). ^{13}C NMR (100 MHz, $CDCl_3$) δ 188.7, 177.7, 166.0, 157.7, 145.9, 143.0, 134.2 (q, J = 32.2 Hz), 132.2, (q, J = 32.4 Hz), 130.9, 129.7 (2C), 126.9 (2C), 125.8 (q, J = 280 Hz, CF_3), 125.4, (2C) 121.6, 116.2 (2C), 91.9, 63.9, 61.7, 59.4, 56.6, 53.6, 47.7, 38.9, 34.4, 21.6. Analysis calculated for $C_{29}H_{29}F_6N_5O_5S$; C, 51.71; H, 4.34; F, 16.92; N, 10.40; O, 11.88; S, 4.76; found C, 51.91; H, 4.32; F, 16.92; N, 10.37; O, 11.88; S, 4.76; LCMS: m/z = 674.1 $[M + H]^+$.

(2-((2-(2-(Methylsulfonyl)-2,6-dihydropyrrolo[3,4-*c*]pyrazol-5(4*H*)-yl)acetyl)thio)-6-(trifluoromethyl)-4-(4-(trifluoromethyl) phenyl)-1,4-dihydropyrimidine-5-carbonyl)histidine (12h)

Light brown solid, yield = 48%, m.p. 231–233 °C; R_f = 0.46; (*n*-hexane/EA; 3 : 1); HPLC purity = 97.6% (C18 RP, acetonitrile/H_2O-80 : 20), TR = 13.3 min. ^{1}H NMR (400 MHz, DMSO-d_6) δ 12.01 (s, 1H, COOH, His), 9.46 (s, 1H, py-NH), 8.68 (s, 1H, imidazole, NH), 8.53 (s, 1H, CONH, His), 7.94 (s, 1H, pyrazol–ArH), 7.79 (s, 1H, imidazole, ArH), 7.75 (d, J = 8.16 Hz, –2H, ArH), 7.24 (d, J = 8.16 Hz, –2H, ArH), 7.10 (s, 1H, imidazole, ArH), 5.28 (s, 1H, –CH), 4.34–4.29 (m, 1H, $CHCH_2$, His), 4.19–4.14 (m, 4H, 2× CH_2), 3.48–3.42 (m, 2H, $CHCH_2$, His), 3.10 (s, 3H, SO_2–CH_3), 3.01 (s, 2H, CH_2). ^{13}C NMR (100 MHz, $CDCl_3$) δ 189.8, 175.3, 164.5, 150.8, 144.9, 142.4, 138.8, 135.2, 133.5 (q, J = 36.6 Hz, –C–CF_3), 131.2 (q, J = 36.1 Hz, –C–CF_3), 130.6, 130.4, 127.5, 126.1, 125.7, 125.2 (q, J = 272.8 Hz, –CF_3), 124.9, 124.4, 123.0, 122.8, 118.8, 90.7, 63.8, 57.2, 55.4, 54.6, 54.0, 41.0, 29.6. Analysis calculated for $C_{27}H_{24}F_6N_8O_6S_2$; C, 44.14; H, 3.29; F, 15.52; N, 15.25; O, 13.07; S, 8.73; found C, 44.11; H, 3.31; F, 15.52; N, 15.22; O, 13.07; S, 8.73; LCMS: m/z = 735.12 $[M + H]^+$.

(2-((2-(2-(Methylsulfonyl)-2,6-dihydropyrrolo[3,4-*c*]pyrazol-5(4*H*)-yl)acetyl)thio)-6-(trifluoromethyl)-4-(4-(trifluoromethyl) phenyl)-1,4-dihydropyrimidine-5-carbonyl)-L-tyrosine (12i)

Off white solid, yield = 49%, m.p. 221–223 °C; R_f = 0.47; (*n*-hexane/EA; 3 : 1); HPLC purity = 97.7% (C18 RP, acetonitrile/H_2O-80 : 20), T_R = 13.4 min. ^{1}H NMR (400 MHz, DMSO-d_6) δ 12.28 (s, 1H, COOH, Tyr), 9.45 (s, 1H, py-NH), 9.24 (s, 1H, Tyr–OH), 8.50 (d, J = 2.64 Hz, 1H, CO–NH), 7.83 (s, 1H, pyrazol–ArH), 7.76 (d, J = 7.88 Hz, –2H, ArH), 7.24 (d, J = 8.72 Hz, –2H, ArH), 7.04 (d, J = 7.6 Hz, 2H, Tyr–ArH), 6.75 (d, J = 7.48 Hz, 2H), 5.29 (s, 1H, –CH), 4.94–4.89 (m, 1H, $CHCH_2$ of Tyr), 4.20–4.13 (m, 4H, 2× CH_2), 3.66 (dd, 1H, J = 12.12 Hz, J = 9.64 Hz, CH_2 of Tyr), 3.48 (dd, 1H, J = 11.92 Hz, J = 5.04 Hz, CH_2 of Tyr), 3.12 (s, 3H, CH_2), 2.98 (s, 2H, CH_2). ^{13}C NMR (100 MHz, DMSO-d_6) δ 189.8, 174.9, 164.5, 156.4, 150.8, 144.9, 142.4, 132.3, 132.0, 132.4 (q, J = 36.9 Hz, –C–CF_3), 131.8 (q, J = 36.3 Hz, –C–CF_3), 129.6, 127.5, 126.1, 125.7, 125.2, 124.9, 124.4, 123.6, 122.5 (q, J = 273 Hz, –CF_3), 115.8, 90.7, 63.8, 57.2, 55.4, 55.0, 54.6, 41.0, 37.2. Analysis calculated for $C_{30}H_{26}F_6N_6O_7S_2$; C, 47.37; H, 3.45; F, 14.99; N, 11.05; O, 14.72; S, 8.43; found C, 47.19; H, 3.46; F, 14.99; N, 11.02; O, 14.72; S, 8.43; LCMS: m/z = 761.1 $[M + H]^+$.

(2-((2-(2-(Methylsulfonyl)-2,6-dihydropyrrolo[3,4-*c*]pyrazol-5(4*H*)-yl)acetyl)thio)-4-(4-nitrophenyl)-6-(trifluoromethyl)-1,4-dihydro pyrimidine-5-carbonyl)-L-glutamic acid (12j)

Yellow solid, yield = 56%, m.p. 234–236 °C; R_f = 0.41; (DCM/MeOH; 5 : 1); HPLC purity = 97.8% (C18 RP, acetonitrile/H_2O-80 : 20), T_R = 9.1 min. ^{1}H NMR (400 MHz, DMSO-d_6) δ 12.36 (s, 1H, COOH), 11.70 (s, 1H, COOH), 9.36 (s, 1H, py-NH), 8.44 (d, J = 4.4 Hz, –NH), 8.26 (d, J = 8.7 Hz, 2H, ArH), 7.95 (d, J = 8.7 Hz, 1H, pyrazol–ArH), 7.76 (s, 2H, ArH), 5.47 (s, 1H, –CH), 4.52–4.42 (m, 1H, glu), 4.24–4.22 (m, 4H, 2× CH_2), 3.12 (s, 3H, SO_2–CH_3), 2.97 (s, 2H, CH_2), 2.31 (t, J = 7.24 Hz, 2H, glu), 2.29–1.92 (m, 2H, glu). ^{13}C NMR (100 MHz, DMSO-d_6) δ 188.3, 177.0, 176.5, 151.7, 146.4, 145.7, 131.8 (q, J = 32.5 Hz, C–CF_3), 129.0, 126.4 (q, J = 273.1 Hz, CF_3), 124.5, 124.0, 123.7, 121.2, 91.7, 64.9, 56.0, 55.1, 48.9, 41.9, 32.6, 23.8. Analysis calculated for $C_{25}H_{24}F_3N_7O_{10}S_2$; C, 42.68; H, 3.44; F, 8.10; N, 13.93; O, 22.74; S, 9.11; found C, 42.53; H, 3.45; F, 8.10; N, 13.97; O, 22.74; S, 9.11; LCMS: m/z = 704.1 $[M + H]^+$.

4-(2-((2-(2-(Methylsulfonyl)-2,6-dihydropyrrolo[3,4-*c*]pyrazol-5(4*H*)-yl)acetyl)thio)-4-(4-nitrophenyl)-6-(trifluoromethyl)-1,4-dihydropyrimidine-5-carboxamido)benzene-sulfonic acid (12k)

Brownish solid, yield = 64%, m.p. 254–256 °C; R_f = 0.43; (*n*-hexane/EA; 3 : 1); HPLC purity = 97.6% (C18 RP, acetonitrile/H_2O-80 : 20), T_R = 12.5 min. ^{1}H NMR (400 MHz, $CDCl_3$) δ 10.15 (s, 1H, SO_2–OH), 9.42 (s, 1H, py-NH), 8.49 (s, 1H, CO–NH), 8.32 (d, J = 8.9 Hz, 2H, ArH), 8.23 (d, J = 8.4 Hz, 2H, ArH), 7.89 (d, J = 8.1 Hz, 2H, ArH), 7.87 (s, 1H, pyrazol–ArH), 7.86 (d, J = 8.4 Hz, 2H, ArH), 5.41 (s, 1H, –CH), 4.17–4.17 (m, 4H, 2× CH_2), 3.11 (s, 2H, CH_2), 3.09 (s, 3H, SO_2–CH_3). ^{13}C NMR (100 MHz, $CDCl_3$) δ 189.8, 166.1, 150.8, 147.3, 144.9, 140.7, 136.3, 133.1, 132.8 (q, J = 32.8 Hz, –C–CF_3), 129.6, 128.0, 124.7, 123.1, 122.5, 121.3, 119.8, 100.1, 64.2, 57.4, 56.0, 55.8, 41.0. Analysis calculated for $C_{26}H_{22}F_3N_7O_9S_3$; C, 42.80; H, 3.04; F, 7.81; N, 13.44; O, 19.73; S, 13.18; found C, 42.93; H, 3.05; F, 7.81; N, 13.48; O, 19.73; S, 13.18, LCMS: m/z = 730.0 $[M + H]^+$.

(4-(4-(Methoxycarbonyl)phenyl)-6-(trifluoromethyl)-2-((2-(3-(tri fluoromethyl)-5,6-dihydro-[1,2,4]triazolo[4,3-*a*]pyrazin-7(8*H*)-yl) acetyl)thio)-1,4-dihydropyrimidine-5-carbonyl)-L-histidine (12l)

White solid, yield = 57%, m.p. 195–197 °C; R_f = 0.44; (DCM/MeOH; 5 : 1); HPLC purity = 98.6% (C18 RP, acetonitrile/H_2O-80 : 20), T_R = 8.8 min. ^{1}H NMR (400 MHz, DMSO-d_6) δ 12.01 (s, 1H, COOH, His), 9.53 (s, 1H, py-NH), 8.69 (s, 1H, imidazole, NH), 8.53 (s, 1H, CONH, His), 7.94 (s, 1H, imidazole, ArH), 7.92 (d, J = 8.6 Hz, 2H, ArH), 7.44 (d, J = 8.7 Hz, 2H, ArH), 7.10 (s, 1H, imidazole, ArH), 5.28 (s, 1H, –CH), 4.35–4.30 (m, 1H, $CHCH_2$, His), 4.35 (t, 2H, pip-CH_2), 3.92 (s, 3H, –OCH_3), 3.79 (s, 2H, CH_2), 3.41–3.48 (m, 2H, $CHCH_2$, His), 3.31 (s, 2H, pip-CH_2), 3.26 (t, 2H, pip-CH_2), 2.33 (t, 3H, CH_3). ^{13}C NMR (100 MHz, DMSO-

d_6) δ 188.7, 175.3, 168.0, 164.5, 148.8, 145.4, 144.9, 140.5, 140.2, 138.8, 135.2, 132.8, 132.6 (q, J = 32.4 Hz, –C–CF_3), 132.5 (q, J = 36.0 Hz, –C–CF_3), 129.6, 124.9, 123.6, 122.8, 118.8, 117.7, 115.6, 90.7, 61.3, 56.9, 54.0, 52.8, 52.1, 49.8, 42.7, 29.6. Analysis calculated for $C_{28}H_{25}F_6N_9O_6S$; C, 46.09; H, 3.45; F, 15.62; N, 17.28; O, 13.16; S, 4.39; found C, 45.91; H, 3.46; F, 15.62; N, 17.33; O, 13.16; S, 4.39; LCMS: m/z = 730.1 $[M + H]^+$.

Docking studies

Docking studies were conducted by AutoDock4 version (v4.2.6). The crystal structure of SARS-CoV-2 M^{pro}, along with its native ligand, was retrieved from the Protein Data Bank (PDB) with accession code **6XHM**, which offers the target's highest resolution. The docking protocol was adapted from established procedures. The chemical structures of the designed intermediates and inhibitors were sketched using ChemDraw software, followed by geometry optimization, and energy minimization with the Avogadro tool using the MMFF94 force field. Optimized structures were saved in PDB format and converted to PDBQT format using AutoDock Tools (ADTs) with appropriate torsion settings and flexible bonds. Upon ligand preparation, the protein was downloaded from PDB and underwent pre-docking optimization, which included the removal of water molecules, addition of hydrogen atoms, and assigning of Kollman charges. The protein was first saved in PDB format followed by conversion to PDBQT format *via* ADTs. The active site of protein (**6XHM**) was identified based on coordinates (*X*: 10.541898, *Y*: 14.409504, *Z*: 27.098183), obtained using Discovery Studio Visualizer v24.1.0.23298. A grid box with the blind dimensions was set to encompass the entire ligand, ensuring sufficient coverage for binding conformations sampling. The file is saved in .gpf format. Docking parameters were defined using genetic algorithm configurations with 10 runs and 2 500 000 energy evaluations per run. AutoDock4 version (v4.2.6) was employed for docking simulations, which predicted binding energies. The resulting .dpf file was generated and subsequently used to produce .glg and .dlg files.[40,41] A more favorable pose is associated with a lower score and the scoring function used kcal per mole as the unit. After docking, protein–ligand interactions, including H-bonding, π–π stacking, π–sigma stacking, *etc.*, were analyzed using 2D and 3D visualization through Discovery Studio Visualizer v24.1.0.23298.[42]

Methodology of SARS-CoV-2 M^{pro} assay

The *in vitro* enzymatic inhibition assay was conducted using the SARS-CoV-2 M^{pro} Inhibitor Screening Assay Kit supplied by BPS Biosciences. This assay provides a reliable and user-friendly platform for evaluating potential inhibitors of M^{pro}. The assay followed the manufacturer's recommended protocols and was performed using a 96-well plate format. Inhibitor solutions were prepared by diluting the synthesized compound into the M^{pro} assay buffer. The assay utilized a fluorogenic substrate containing a cleavage site between nsp4 and nsp5, which, under normal conditions, is cleaved by M^{pro}. The cleavage released the EDANS fluorophores for the Dabcyl quencher, producing a measurable fluorescent signal. Fluorescence intensity was measured using a PerkinElmer 2030 Victor X Multilabel Plate Reader with excitation and emission wavelengths set to 355 nm and 535 nm, respectively. **GC376**, a known M^{pro} inhibitor, was included as a standard reference drug. In the 1st step, 5 ng of MBP-tagged M^{pro} enzyme was combined with 30 μL of assay buffer containing 1 mM dithiothreitol (DTT). Synthesized compounds dissolved in DMSO (10 μL) were added to the mixture and pre-incubated for 1 h at rt. Subsequently, 10 μL of the fluorescent substrate was added to initiate the enzymatic reaction, bringing the final reaction volume to 50 μL. The final concentration of the substrate and inhibitor in the reaction mixture was maintained at 50 μL. The incubation was carried out at rt for 12–17 hours. The assay tested a range of inhibitor concentrations (0.005–50 μL) to determine IC_{50} values. Positive control of well-containing enzymes, 1% DMSO, and substrate showed no inhibition of enzymatic activity. As reference control **GC376** inhibitor was tested at 100, 10 and 0.1 μM. The IC_{50} values of the synthesized compounds were calculated using the nonlinear regression (curve fit) function in the GraphPad Prism 8.0 software.[43]

M^{pro} cytotoxic assay

The cytotoxic activity of the synthesized compounds was assessed in Vero-E6 cells using the MTT assay with minor modifications. Stock solutions of the compounds were initially dissolved in 10% aqueous DMSO solution, followed by further dilution in DMEM to prepare working solutions. Vero-E6 cells were seeded in 96-well plates at a density of 1×10^4 cells per well and incubated for 24 hours at 37 °C in the five percent CO_2 atmosphere. Various concentrations of the synthesized compound were then applied to the cells, and they were incubated for 48 hours under the same conditions. Cytotoxicity was determined by adding 10 μL of MTT reagent (5 mg mL^{-1} in PBS) to each well, followed by additional incubation for 4 hours to allow formazan crystal formation. The resulting crystals were dissolved in 100 μL of DMSO, and absorbance was measured at 570 nm using a microplate reader.[44] The percentage of cell viability was plotted against the compound concentration, and the 50% cytotoxic concentration (CC_{50}) was subsequently calculated using the non-linear regression function in GraphPad Prism 8.0.[43,45,46]

Molecular dynamic simulation

After docking studies, the best and most potent COVID-19 inhibitor and conformation were selected for the molecular dynamic simulation (MDS) to evaluate their interaction at the molecular level and in real body conditions. GROMACS software was used to perform molecular dynamic simulation. Charmm GUI server was used to generate input files for MD simulation. The protein–ligand complex was enclosed in a cubic box and solved using the TIP3P water model. The system was equilibrated with a human body temperature at 37 °C and 1 atm pressure. The system was minimized using 50 000 steps before performing MD simulation.

After MD simulation, root means square deviation (RMSD) analysis of protein and complex backbone has been performed

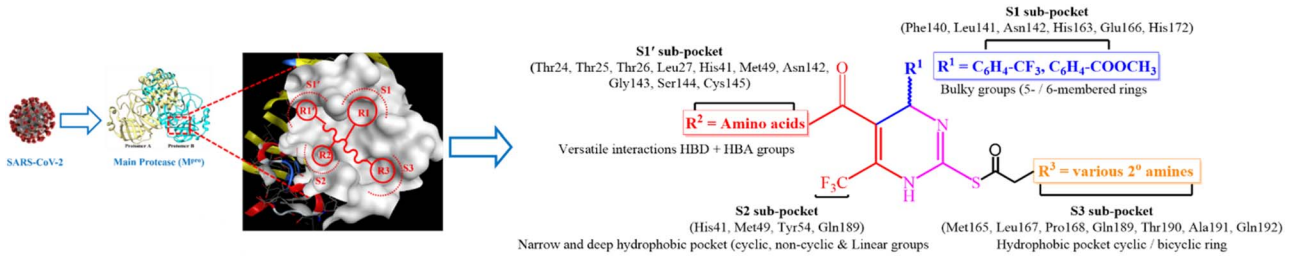

Fig. 4 Design strategy for SARS-CoV-2 M^{pro} inhibitors.

to evaluate the structural changes of protein before and after ligand inhibition. RMSD gives a clear picture of overall protein dynamics (such as folding and unfolding) and conformational changes during the MD simulation. On the other hand, the Root Mean Square Fluctuation (RMSF) calculation analyzes the movement/fluctuation of protein regions and residue during the simulation. Another key parameter to understand the ligand inhibition potential and protein–ligand complex at the molecular level is the number of hydrogen bonding interactions throughout simulations.

Results and discussion

Design rational

We have conducted a comprehensive literature review on the surface topology of the M^{pro} active site and existing M^{pro} inhibitors (repurposed and rationalized). DHPM-based inhibitors have demonstrated anti-HIV,[47,48] anti-SARS-CoV-1,[49–51] and anti-SARS-CoV-2 (ref. 49, 50 and 52–54) properties. Due to the notable pharmacological relevance, we focused on DHPM's derivatives featuring EWGs and EDGs to design M^{pro} inhibitors. Our laboratory has previously explored the DHPM scaffold and reported its diverse activity profiles targeting various biological assays.[55–61] We designed and docked DHPM derivatives against the best resolution X-ray crystallographic structure of the M^{pro} (PDB id: **6XHM**), identified three promising DHPM-2-thiones (**6a–c**) with the lowest binding energies as a hit for guiding our lead identification process. To refine these hits, SAR analysis was employed to delineate critical structural elements that enhance biological activity. Subsequently, lead compounds (**8a–h**) were docked, and their IC_{50} values were determined (Fig. 5). This systematic approach enables precise lead optimization. The M^{pro} comprises four pockets S1, S1′, S2, and S3 pockets. Notable inhibitors such as N3, **13b**, **11a**, **11b**, X77, boceprevir, and dipyridamole include five- and six-membered rings, showcasing the S1 pocket's capacity to accommodate bulky substituents.[62,63] The S1′ pocket is the hydrated region within the active site that forms a water bridge with Thr26, and requires proton donors and acceptors, essential to maintain the water bridge in S1′ and H-bond within S1, inhibitors lacking these groups often exhibit reduced activity. The NGSC motif (Asn142–Gly143–Ser144–Cys145) in S1′ is crucial for forming H-bonds with inhibitors.[64–66] The S2 pocket of M^{pro} is deeply embedded in nature, favoring six-membered ring and halogenated moieties enhancing bindings affinities *e.g.* nirmatrelvir, **13b** and **11b**.[63] The hydrophobic S3 pocket supports cyclic structures and branched alkyl chains (*e.g.* X77, **11a**, PF-00835231, boceprevir, and **13b**),[63] with full occupancy observed for six-membered ring.[67] In line with these findings, we synthesized DHPM derivatives with proton donor/acceptor groups, aromatic bicyclic moieties, aliphatic moieties, and six-membered rings to optimize interactions across M^{pro}. Additionally, we strategically incorporated fluorine into our inhibitors, a modification known to increase the inhibitory potency of various medications such as anti-HIV (*e.g.* efavirenz) and antivirals (*e.g.* raltegravir, emtricitabine, ledipasvir, and tenofovir). Its presence is particularly relevant to the S1, S2, and S3 pockets where its electronegativity enhances the H-bonding and hydrophobic interactions, improving binding affinity.[68] The synthesis of these potent compounds was carried out. To validate *in silico* findings, *in vitro* analysis was conducted confirming biological activity safety & efficacy. These results provided quantitative data for further optimization in drug development (Fig. 4).

Chemistry

In the present study, we have synthesized a series of DHPM-based SARS-CoV-2 M^{pro} inhibitors. Initially, a range of aromatic aldehydes, thiourea and ethyl 4,4,4-trifluoro-3-oxobutanoate underwent a multi-component, one-pot classical Biginelli reaction in the presence of tin(II) chloride catalyst, leading to the formation of a variety of substituted DHPM-thiones (**6a–c**) (Scheme 1).

Subsequently, DHPM-thione derivatives reacted with various primary amines *via* a substitution reaction, resulting in the

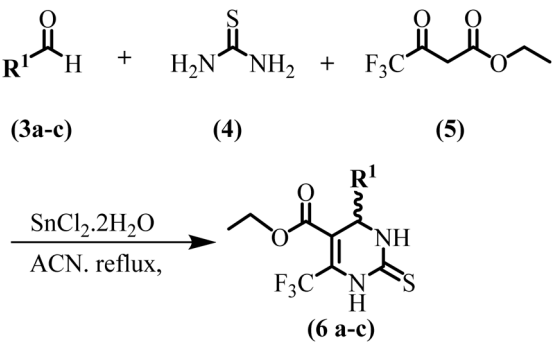

Scheme 1 DHPM-thiones (**6a–c**) synthesis through Biginelli reaction.

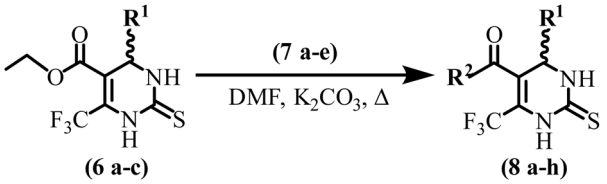

Scheme 2 Synthesis of DHPM-thiones amide derivatives (**8a–h**) by reaction of DHPM's & 1° amines.

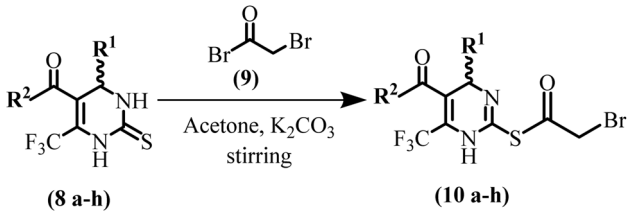

Scheme 3 Bromoacetylated DHPM-thiones (**10a–h**) synthesis by reaction of (**8a–h**) with (**9**).

synthesis of amide derivatives of DHPM-thiones (**8a–h**) (Scheme 2).

In the next step, bromoacetylated DHPM-thione (**10a–h**) (Scheme 3) were prepared through the reaction of amide derivatives of DHPM-thione with bromoacetyl bromide.

Finally, potent SARS-CoV-2 inhibitors (**12a–l**) based on DHPM-thiones scaffold were synthesized by reacting the bromoacetylated DHPM-thiones with diverse secondary amines (Scheme 4).

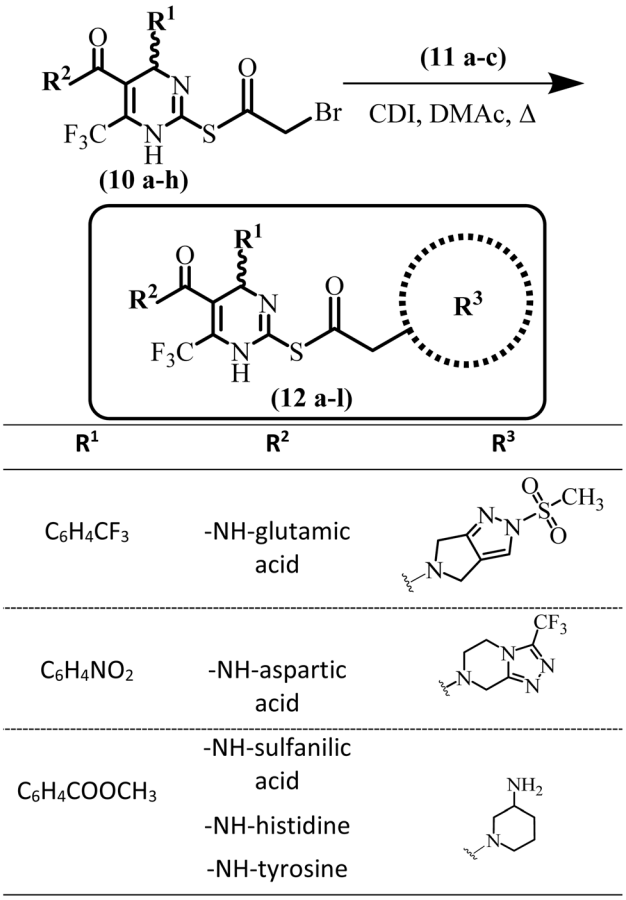

Scheme 4 Reaction of bromoacetylated products (**10a–h**) with diverse 2° amines.

In vitro pharmacology [inhibitory concentrations (IC_{50}) and cytotoxicity concentration (CC_{50})]

The M^{pro} of SARS-CoV-2 plays a critical role in the virus replication by cleaving viral polyproteins, making it a pivotal target for the therapeutic intervention. Numerous covalent and non-covalent inhibitors such as carmofur, PX-12, and **GC376** have been developed to combat SARS-CoV-2. These inhibitors feature N-heterocycles, that mimic the glutamine amino acid at P1 active site. Covalent inhibitors target the catalytic Cys145 residue leading to potent antiviral activity through both cellular and enzymatic inhibition. Noteworthy, ML188.47, a non-covalent M^{pro} inhibitor, has demonstrated significant efficacy against M^{pro}.[69–71]

In this study we identified lead compounds through comprehensive Structure–Activity Relationship (SAR) analysis, followed by their optimization. Various amino acids were conjugated on the western side of the DHPM-thione scaffold using different synthetic strategies. The half-minimal inhibitory concentration (IC_{50}) values of these intermediates were determined using M^{pro} assay kit. The *in vitro* inhibition results of the intermediates are summarized in Fig. 5. SAR analysis revealed that intermediate **8a** containing a trifluoromethyl benzene moiety on the northern side and glutamic acid at the western side of scaffold DHPM-thione, exhibited potent inhibitory activity with an IC_{50} of 23.2 μM ± 0.92. Substituting glutamic acid with aspartic acid in **8b** reduced inhibitory activity (IC_{50} = 44.7 ± 1.36 μM), indicating that the carbon chain length influences inhibition. Conjugation with sulfanilic acid in **8c** enhanced inhibitory potency (IC_{50} = 28.2 μM ± 1.71). Based on these findings, we hypothesized that cyclic moieties could enhance activity. Replacing sulfanilic acid with histidine in **8d** resulted in a marginally altered IC_{50} of 30.7 μM ± 1.43 while substituting with tyrosine in **8e** yielded a significant inhibitory effect (IC_{50} = 25.3 μM ± 1.02). Modifying the northern side with nitrobenzene, while retaining glutamic acid in **8f** and sulfanilic acid in **8g** on the western side, resulted in reduced potency, with IC_{50} values of 36.8 μM ± 1.36 and 55.5 μM ± 1.43 respectively. Further SAR exploration incorporating histidine (**8h**) at the western side, paired with methyl benzoate at the northern side resulted in IC_{50} values of 34.9 μM ± 1.042 μM. The histidine derivative **8h** demonstrated superior inhibitory activity. In conclusion, the SAR analysis highlights the critical role of cyclic moieties on the western side of the DHPM-thione scaffold, along with strategic substitution on the northern side, in influencing the inhibitory efficacy against the SARS-CoV-2 M^{pro}. This SAR investigation underscores the potential of strategic substitution to enhance the potency of M^{pro} inhibitors (Fig. 5).

In our study, we synthesized a series of dihydropyrimidine-2-thione-based compounds (**12a–l**) based on SAR insights and evaluated *in vitro* inhibitory potential against SARS-CoV-2 M^{pro}.

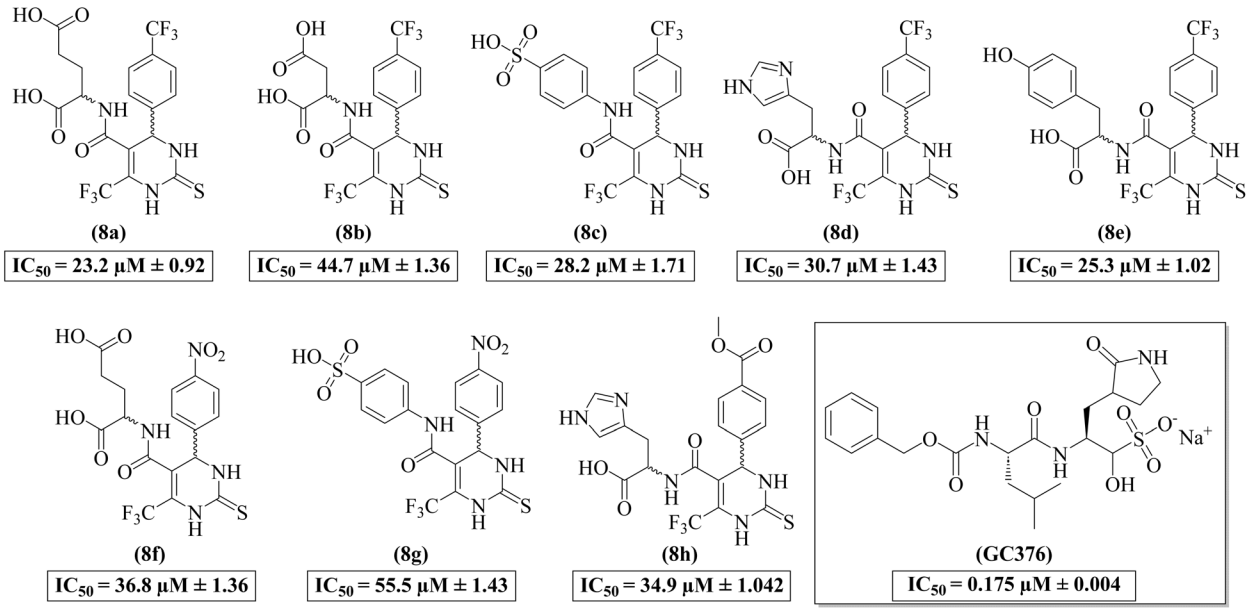

Fig. 5 Intermediates (8a–h) synthesized during the SARS-CoV-M^{pro} inhibitor development and standard drug GC376.

GC376 (a well-known SARS-CoV-2 inhibitor) was used as a benchmark to compare the *in vitro* results. Several exhibited notable inhibitory activities at the sub-micromolar range against SARS-CoV-2 M^{pro}, ranging from moderate to excellent.

Notably, compound **12l** demonstrated remarkable potency, with an IC_{50} value of 0.054 μM ± 0.001, significantly surpassing the benchmark inhibitor **GC376** (IC_{50} = 0.175 μM ± 0.004). The incorporation of histidine on the western side of **12l** provided a key structure–activity relationship (SAR) insight essential for M^{pro} inhibition. However, contrary to expectations, (**12d**) and (**12h**), which also features histidine, exhibited lower inhibitory activity (IC_{50} = 14.38 μM ± 1.05 and 16.27 μM ± 0.81, respectively), suggesting that additional structural elements critically modulate efficacy.

The methyl benzoate moiety at the northern side of **12l** further contributed to its enhanced activity, underscoring its importance in M^{pro} inhibition. Additionally, halogenated substituents, particularly fluorine, on the northern side influenced inhibitory potential across (**12a–i**). While most fluorinated compounds, including (**12b**), (**12c**), (**12d**), (**12f**), and (**12h**), displayed limited activity, compounds (**12a**), (**12e**), (**12g**), and (**12h**) exhibited improved inhibition (IC_{50} = 0.15 μM ± 0.01, 0.73 ± 0.04, 0.21 ± 0.01, and 16.27 μM ± 0.81, respectively) relative to **GC376**. The IC_{50} values for (**12a–l**) are summarized in Fig. 6.

Furthermore, (**12a**) and (**12e**) display superior efficacy when combined with additional functional groups, such as glutamic acid and tyrosine, on the western side. Further lead optimization revealed that **12j** (IC_{50} = 0.063 μM ± 0.001) and **12k** (IC_{50} = 0.146 μM ± 0.001) exhibited excellent inhibitory activity. These derivatives leveraged glutamic and sulfanilic acid moieties on the western side and nitrogen- and sulfur-containing groups on the northern and eastern sides, respectively.

The exceptional potency of compound **12l** was attributed to the fluorinated triazolo-pyrazine group on its eastern side, a feature also observed in the potent **12a** and **12e**. Moreover, the piperidinyl amine group in (**12g**) and the sulfonyl pyrrolo-pyrazole moiety in **12i**, **12j**, and **12k** further enhanced inhibition. These findings underscore the critical role of diverse substituents including histidine, halogens (fluorine), and functional groups containing nitrogen, oxygen, and sulfur in optimizing the efficacy of M^{pro} inhibitors.

Notably, compounds **12a**, **12j**, **12k**, and **12l** outperformed **GC376** in M^{pro} inhibition, while others displayed moderate to good activity. Among the most potent inhibitors, **12j** and **12l** each achieved over 50% inhibition against M^{pro}. Dose–response experiments for **12j**, **12k**, and **12l** confirmed their IC_{50} values, as depicted in Fig. 7. Compound **12l** emerged as a highly promising candidate, demonstrating exceptional inhibitory potency against SARS-CoV-2 M^{pro}, making it a viable candidate for further drug development.

The cytotoxic potential of the synthesized DHPM-2-thione derivatives were evaluated to determine their half-maximal cytotoxic concentration (CC_{50}) against SARS-CoV-2. The MTT assay revealed a wide spectrum of cytotoxic responses among the compounds, ranging from low to high. By employing non-linear regression analysis, the data were converted into the percent cell viability, enabling the precise calculation of CC_{50} values. Furthermore, these values were utilized to compute the selectivity index (SI) as the ratio of CC_{50} to IC_{50}, providing insight into the therapeutic safety margins of the compounds.

The IC_{50} and CC_{50} graphs for the compounds are summarized in Fig. 7 and 8 respectively. Among these compounds, (**12c**) exhibited the highest CC_{50} of 247 μM, (lowest cytotoxicity) followed by **12k** (CC_{50} = 239 μM), **12i** (CC_{50} = 243 μM), **12j** (CC_{50} = 211 μM) and **12l** (CC_{50} = 198 μM). Particularly, structural optimization contributed significantly to improving CC_{50} values for selected derivatives, highlighting the critical role of the chemical modifications in enhancing their safety profiles. The

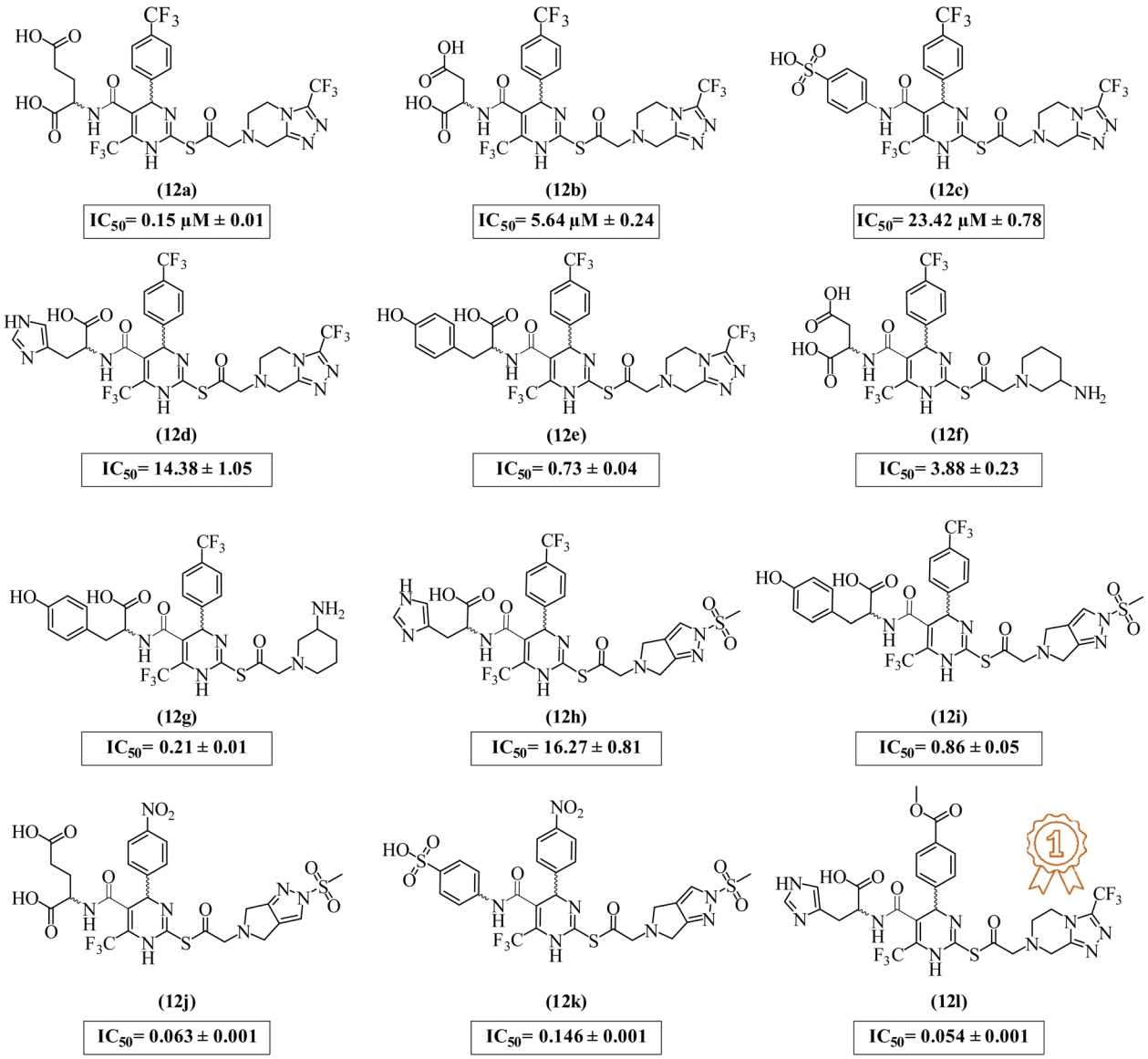

Fig. 6 *In vitro* M^{pro} inhibition results of synthesized compounds **12a–l**.

CC_{50} value for these compounds, as observed on Vero E6 cells, offers a detailed comparison of their cytotoxic profile.

Docking studies

Docking studies were conducted to thoroughly analyze the spatial orientation and binding configurations of ligand–enzyme complexes. The crystal structure of the M^{pro}, co-crystallized with native ligands *N*-[(2*S*)-1-({(2*S*,3*S*)-3,4-dihydroxy-1-[(3*S*)-2-oxopyrrolidin-3-yl]butan-2-yl}amino)-4-methyl-1-oxopentan-2-yl]-4-methoxy-1*H*-indole-2-carboxamide and EDO (1,2-ethanediol), was retrieved from the Protein Data Bank (PDB) under accession code **6XHM**, featuring the best resolution. To confirm the reliability of the docking protocol, a re-docking of the native ligand with the M^{pro} was performed. The observed root-mean-square deviation (RMSD) values were <2.0 Å, indicating a high degree of consistency between the experimental and modelled configurations.

Subsequently, synthesized DHPM-thione derivatives (**12a–l**) were subjected to docking analysis against the binding sites of SARS-CoV-2 M^{pro}, in alignment with SAR study guidelines. Extensive literature reports that M^{pro}/$3CL^{pro}$ comprises four binding pockets: a bulky S1 pocket that accommodates six-member rings and facilitates H-bond formation, a hydrated S1′ pocket, a narrow and hydrophobic S2 pocket and the S3 pocket capable of binding both aliphatic and aromatic moieties. Key amino acid residues involved in the drug design for each pocket include: Phel40, Leul41, Asnl42, Hisl63, Glul66, Hisl72 (S1 pocket); Thr24, Thr25–26, Leu27, His41, Met49, Asnl42, Glyl43, Serl44, Cysl45 (S1′ pocket); His41, Met49, Tyr54, Glnl89, His164, Asp187, Arg188 (S2 pocket); and Metl65, Leul67, Prol68, Glnl89, Thrl90, Alal91, Glnl92, Leu167, Gly170 (S3 pocket).[64,72–80]

To optimize the lead compounds, a detailed SAR analysis was performed against the binding pockets of the M^{pro} using an advanced computational docking approach to assess binding

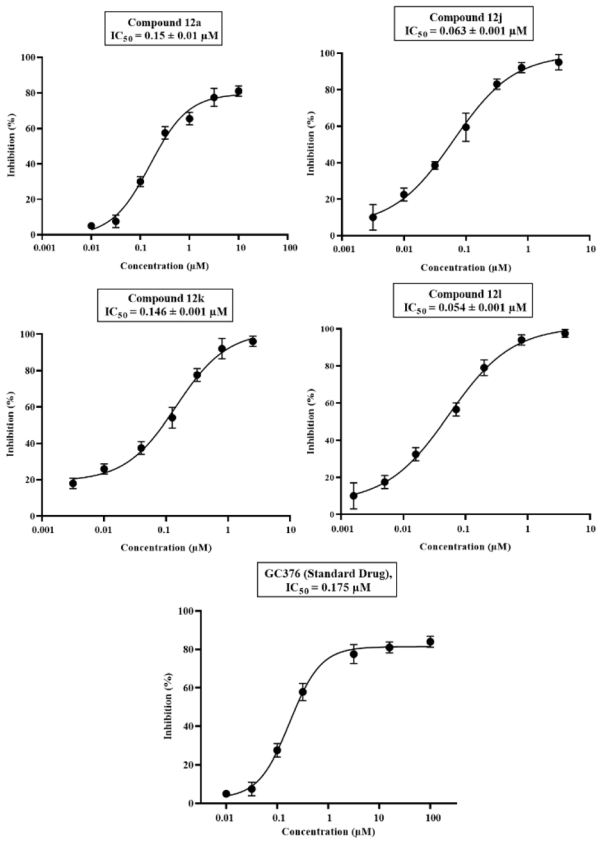

Fig. 7 Dose–response curves for IC_{50} values of compounds **12a**, **12j**, **12k**, **12l**, and standard drug **GC376** ± SEM; $n = 3$.

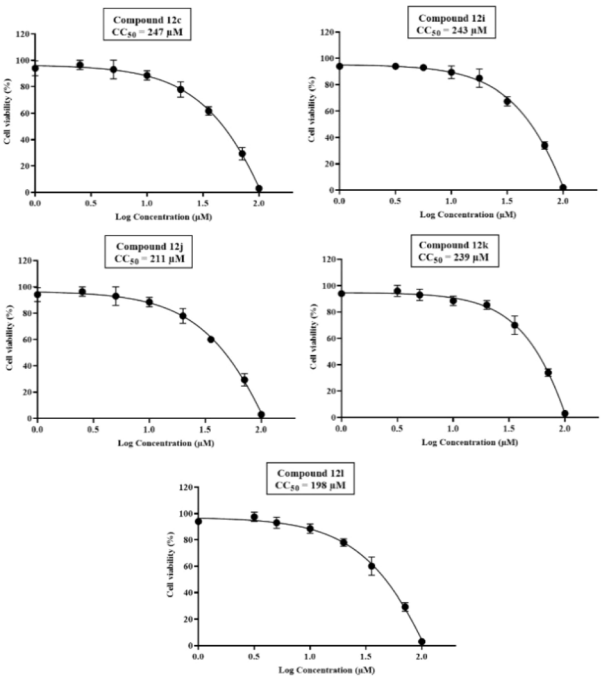

Fig. 8 Half-maximal cytotoxicity concentration (CC_{50}) of final compounds **12c**, **12i**, **12j**, **12k** and **12l** on Vero E6 cell ± SEM; $n = 3$.

interactions and to identify potent intermediate for further inhibitor development. Intermediates (**8a–h**) were docked into M^{pro} binding pockets, with four intermediates (**8a**, **8c**, **8e**, **8h**) showing promising potential. To further enhance the binding affinity of the intermediates, the introduction of additional functional groups is required, which could improve the overall potency of inhibitors.

The 2D interaction plot of intermediate **8a** (Fig. 9(a)) revealed six conventional H-bonds, three halogens (fluorine) interactions, two π–alkyl interactions, and a π–sulfur interaction. Specifically, intermediate **8a** interacted with all four M^{pro} pockets: H-bonds formed with His163, halogen (fluorine) interactions with Phe140 and Leu141, and a π–alkyl interaction with His172 in the S1 pocket. The S1′ pocket exhibited H-bonds and a π–sulfur interaction Ser144 and Cys145 respectively. The S2 pocket showed halogen (fluorine) interactions and H-bonds interactions with His164 and His41, while the S3 pocket displayed H-bond interactions with Gln189 and Thr190 along with a π–alkyl interaction with Met165. The estimated free binding energy value of **8a** in the binding pocket of M^{pro} was −6.9 kcal mol^{-1}, indicating moderate binding affinity and promising potential for further development as an inhibitor.

Intermediate **8c** (Fig. 9(b)) exhibited a similar interaction profile with six conventional H-bonds, three halogens (fluorine) interactions, a π–sulfur and a π–alkyl interaction. H-bond formed with Asn142 and Glu166 in the S1 pocket and with Gly143 in the S1′ pocket. In S2 pocket halogen (fluorine) and π–alkyl interactions were observed with His41, while halogen (fluorine) and π–sulphur interactions with Asp187 and Met49.

The S3 pocket demonstrated H-bond interactions with Glnl89, Thrl90, and Glnl92, along with π–sulphur and π–alkyl interactions with Met49 and Met165 respectively. The estimated free binding energy of the intermediate **8c** was −7.4 kcal mol^{-1}, indicating moderate to strong binding affinity, suggesting its potential for optimization and further investigation as an inhibitor.

The 2D interaction plot for intermediate **8e** (Fig. 10(a)) demonstrated six H-bonds, three halogens (fluorine) interactions, and two π–sulfur interactions. The H-bonds were formed

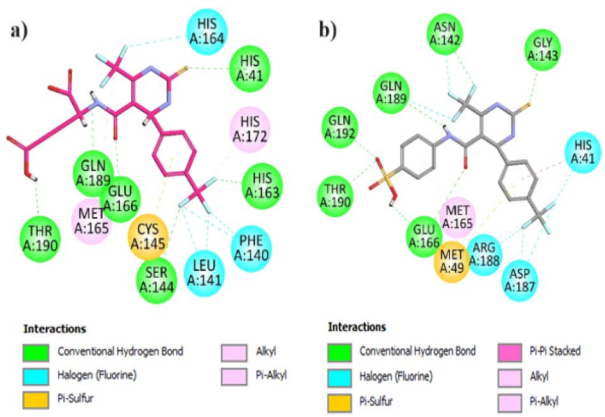

Fig. 9 Two-dimensional (2D) interaction plot of intermediate (a) **8a** (b) **8c**.

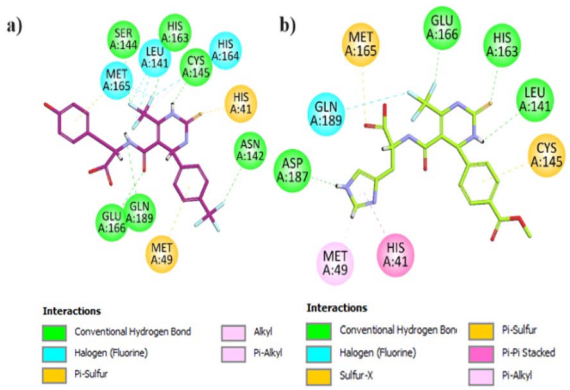

Fig. 10 Two-dimensional (2D) interaction plot of intermediate (a) **8e** (b) **8h**.

with His163, Asn142, and Glu166 in the S1 pocket, while halogen (fluorine) interactions were observed with Leu141. The S1′ pocket H-bonds were formed with Cys145 and Ser144 accompanied by a π–sulfur interaction with Met49. The S2 pocket exhibited halogen (fluorine) interactions with His164 and His41 along with a π–sulfur interaction. The S3 pocket showed halogen (fluorine) interactions with Met165 and an H-bond with Gln189. The estimated free binding energy of the **8e** was −7.3 kcal mol^{-1} indicating moderate to strong binding affinity, suggesting its potential for optimization as an inhibitor.

The 2D interaction plot of intermediate **8h** (Fig. 10(b)) indicated diverse interactions, including four H-bonds, a halogen (fluorine) interaction, one π–sulfur interaction, one sulphur–X interaction, a π–π T shaped interaction, and one π–alkyl interaction. H-bonds were observed with Glu166, HIS163, and LEU141 in S1 pocket. In the S1′ a π–sulfur interaction was noted with Cys145; however, this pocket is not addressed properly as the NGSC motif is not fully engaged. Additionally, the S3 pocket is not occupied comprehensively, suggesting further modifications and indicating the need for further optimization to enhance binding interactions in the pocket. The S2 pocket exhibited a π–π T-shaped interaction with His42, a π–alkyl interaction with Met49 and H-bond with Asp187. The S3 pocket demonstrated halogen (fluorine) interaction with Gln189 and a π–alkyl interaction with Met165. The estimated free binding energy of **8h** was −7.7 kcal mol^{-1} demonstrating highly favorable binding interaction and promising potential for further development as an inhibitor.

The SAR analysis of intermediates **8a**, **8c**, **8e**, and **8h** confirmed their potential as effective M^{pro} inhibitors. These intermediate display robust binding interactions across all four defined binding pockets of SARS-CoV-2 M^{pro}, including H-bonds, halogen (fluorine), π–S, S–X, π–π T-shaped, and π–alkyl, contributing to their high binding affinities. The estimated free binding energies of intermediates ranged from −6.9 to −7.7 kcal mol^{-1} with RMSD values suggesting stable docked conformation. These findings underscore the promising therapeutic potential of these intermediates, warranting further optimization for M^{pro} inhibitors.

The two-dimensional (2D) interaction plot for compound (**12a**), presented in Fig. 11(a) revealed strong binding interactions with M^{pro}. Compound (**12a**) demonstrates versatile interactions with all four defined pockets of M^{pro}, including four halogen–fluorine interactions, six hydrogen bonds (H-bonds), and three π–alkyl interactions. The compound's proton donor and acceptor functionalities enable it to engage key residues across M^{pro}'s pocket. Specifically, in the S1 pocket, (**12a**) forms halogen (F) interactions & π–alkyl interactions with Leu141 and halogen (F) interactions Phe140, H-bonds interaction with Glu166 & His163. In the S1′ pocket, H-bonds were observed with NGSC motif Ser144, and H-bond & π–alkyl interactions were observed with Cys145. In the S2 hydrophobic pocket, halogen (F) interactions & H-bond observed with His164. Furthermore, in the large S3 pocket, which accommodates both cyclic and aliphatic motifs, π–alkyl interactions with Pro168, H-bond observed with Gln189, and halogen (F) interactions were observed with Met165 & Thr190 and the chloro thiophene group. The estimated free binding energy of compound **12a** was calculated to be −10.2 kcal mol^{-1}, indicating a potent inhibitor against M^{pro}. In contrast, compound **12j**, as shown in Fig. 11(b), demonstrated an even more extensive set of interactions with the M^{pro}. This compound formed seven H-bonds, three halogens (F) interactions, and a π–alkyl interaction. The proton donor and acceptor moieties of compound **12j** facilitated its engagement with key residues across all M^{pro} pockets. In the S1 pocket, **12j** formed H-bonds with Asn142 & Glu166, halogen (fluorine) interaction with Leu141 & Phe140, and H-bonds and π–alkyl interaction with His163.

In the S1′ pocket, H-bonds were observed with NGSC residues Ser144, Cys145 & Thr26 involving both carbonyl and fluorine groups. In the S2 pocket H bonding is observed with His164, and in the S3 pocket, Met165 halogen (fluorine) interaction was observed with (trifluoromethyl)benzene. The estimated free binding energy value of **12j** was −11.5 kcal mol^{-1}, reflecting its exceptional binding affinity as an M^{pro} inhibitor. Visual inspection of the docking results revealed that while all synthesized compounds exhibited significant interactions with M^{pro}, compound **12l** displayed the most favorable interactions. It effectively engaged all the key pocket residues and

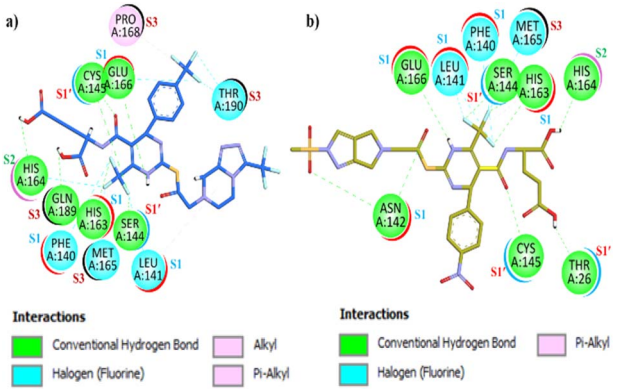

Fig. 11 Two-dimensional (2D) interaction plot of synthesized compound (a) (**12a**) (b) (**12j**).

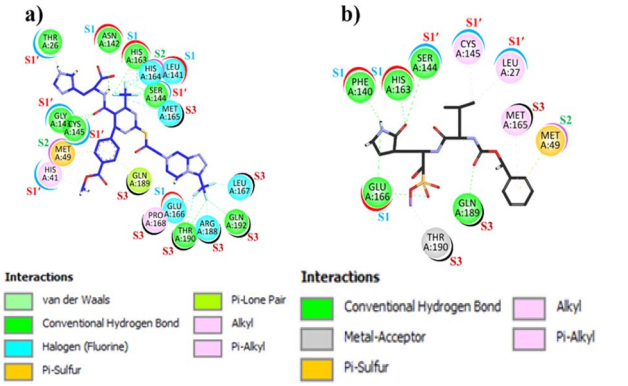

Fig. 12 Two-dimensional (2D) interaction plot (a) synthesized compound (**12l**) (b) referenced drug **GC376**.

demonstrated superior binding affinity compared to the standard drug against M^{pro}. The synthesized compound (**12l**) demonstrated excellent interactions with the SARS-CoV-2 M^{pro}. As shown in Fig. 12(a), a two-dimensional (2D) interaction plot reveals that compound **12l** forms eight conventional H-bonds, six halogen (F) bonds, one π–sulphur interactions, two π–alkyl bonds, and a π–lone pair interaction. The compound comprehensively engages all key residues across all four pockets of M^{pro}. The presence of proton-withdrawing and proton-donating groups in **12l** facilitates H-bonding interactions *via* the carbonyl group and (trifluoromethyl)benzene with key amino acid residues Asnl42, Hisl63. Additionally, halogen (F) bond interactions were observed with residues Glu166 and Leu141 of the S1 pocket, *via* (trifluoromethyl)-triazole and (trifluoromethyl)benzene moieties. In the S1′ pocket, Cys145 forms π–alkyl and conventional H-bond interactions with the carbonyl group and trifluoro moiety. The important residue Thr26 engages *via* H-bonding *via* the imidazole moiety. Furthermore, a π–sulphur interaction with Met49 and H-bonding with Glyl43 and Serl44, facilitated by carbonyl and trifluoro moieties, were also observed. All the NGSC motifs of the S1′ pocket of M^{pro} were effectively addressed by the compound **12l**. In the hydrophobic S2 pocket, π–alkyl interactions with His41, and Met49 were facilitated by the benzene ring, while a π–lone pair interaction with Gln189 was noted. Halogen (F) bond interaction was observed with His164 & Arg188 *via* the trifluoromethyl-triazole moiety. In the S3 pocket Metl65, and Leul67 exhibit halogen (F) interaction through fluorine moiety of DHPM and triazole. Additionally, π–alkyl interaction with Pro168, halogen (F) interaction with Thr190, and H-bonding interaction with Gln192 was observed *via* the trifluoromethyl-triazole moiety in the S3 pocket of the M^{pro} target. The estimated free binding energy for **12l** in the binding pocket of SARS-CoV-2 M^{pro} was -11.9 kcal mol^{-1}, demonstrating a superior binding affinity against M^{pro} making it a highly promising inhibitor. For comparison **GC376** (the standard drug), as shown in Fig. 12(b), exhibited diverse but fewer interactions with M^{pro}. The interactions include five H-hydrogen bond interactions, three π–alkyl bond interactions, a π–sulphur interaction, and one metal acceptor interaction with M^{pro}. **GC376** exhibited H-bond interactions with Phel40, Hisl63, and Glul66 of the S1 pocket residues. In the S1′ pocket, hydrophobic π–alkyl interaction was observed with Leu27 and Cysl45, while H-bonding was observed with Serl44. With the S2 pocket residues Met49 the π–sulphur interaction was observed and with residue Glnl89 the H-bond interactions were observed. In the S3 pocket residue Metl65, hydrophobic interaction π–alkyl was observed while with residue Thrl90 metal acceptor interaction was observed.

Comparative molecular modeling and surface analysis of the intermediate (8h) and final compound (12l)

Our molecular modeling studies revealed that intermediate **8h**, while capable of engaging some key residues, does not comprehensively interact with all four binding pockets of M^{pro}. It fails to fully engage the NGSC motifs in the S1′ pocket and does not extend into the S3 pocket (Fig. 13).

In contrast, the final product **12l** incorporates a trifluoromethyl-triazole moiety that facilitates additional interactions across the S1, S1′, S2, and S3 pockets as shown in Fig. 14. This modification enhances both hydrogen bonding and halogen interactions with residues across all pockets, resulting in the optimal alignment of compound **12l** within the M^{pro} binding clefts. This improvement is reflected in its high inhibitory potency, with an IC_{50} of 0.054 μM, when compared to the intermediate compound **8h**. Overall, our docking analysis *via* surface diagram confirms that the structural modification introduced in **12l** is critical for achieving comprehensive engagement of M^{pro}'s binding pockets and, consequently, for its enhanced antiviral activity.

Molecular dynamic simulations (MDS)

Molecular dynamic simulations of protein and protein–ligand complex were performed to understand the inhibition of our compound at the molecular level and verify the docking results in possible body conditions. Compound inhibition was

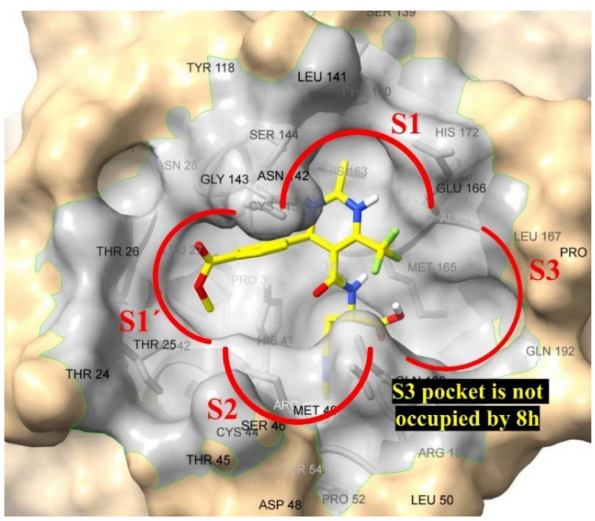

Fig. 13 Interaction of **8h** with the M^{pro} binding sites: the S3 pocket is not occupied by **8h**.

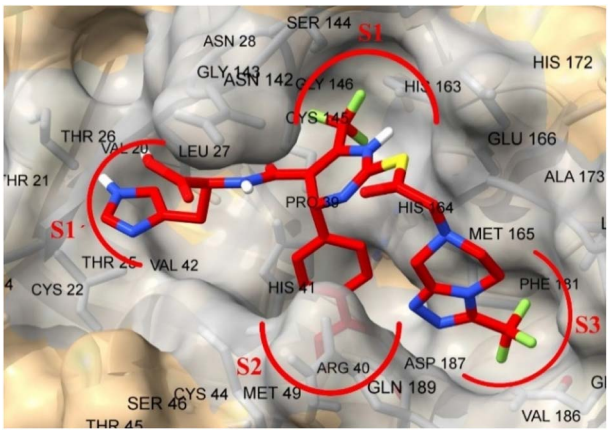

Fig. 14 Comprehensive engagement of **12l** with the M^{pro} binding sites.

analyzed in terms of how it changes or controls the protein overall and regional dynamics as well as their conformation changes. The RMSD graph (Fig. 15) shows that target protein M^{pro} (PDB Id = **6XHM**) shows considerable stability in the first 20 ns and after 20 ns there are so many conformational changes during the simulation which indicates their active conformation changes. The frequency of conformation changes has been reduced in the last 20 ns. The overall RMSD of protein M^{pro} is more than 4 Å. On the other hand, after the binding of the ligand, the protein–ligand complex shows complete stability with RMSD below 2.5 nm throughout the simulation.

The root means square fluctuations (RMSF) (Fig. 16) of target protein **6XHM** and protein–ligand complex are almost similar, with few exceptions in the complex RMSF plot.

The RMSF graph for both is between 0 and 0.6 nm, mostly below 0.2 nm, except for four peaks, which show the flexibility of protein in the ranges of 1–10, 49–55, 190–200, and 290–300. The protein–ligand complex shows more fluctuations at 49–55 and 190–200. Hydrogen bonding analysis was performed to analyze the interaction between the target protein (**6XHM**) and ligand (**12l**).

The histogram (Fig. 17) shows that the minimum number of hydrogen bonds in every frame throughout the simulation is

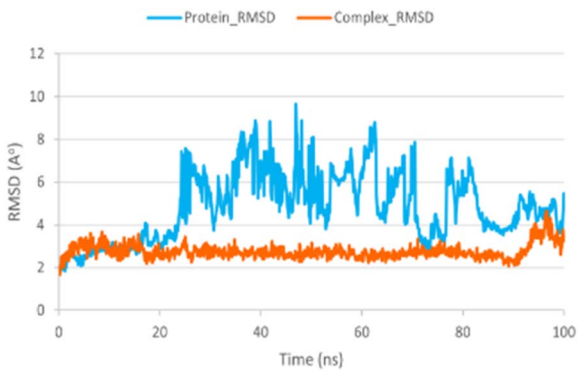

Fig. 15 The root means square deviation (RMSD) graph of protein (blue) and protein–ligand (**12l**) complex (brown).

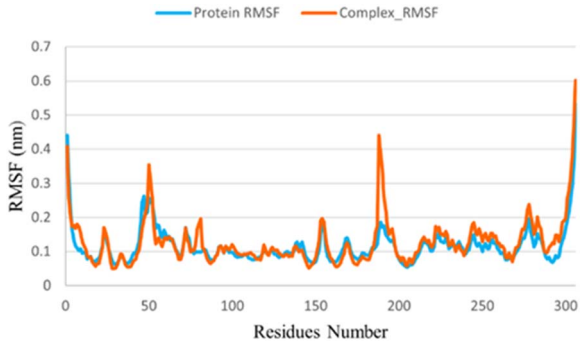

Fig. 16 The root means square fluctuations (RMSF) graph of protein (**6XHM**) (blue) and protein–ligand (**12l**) complex (brown).

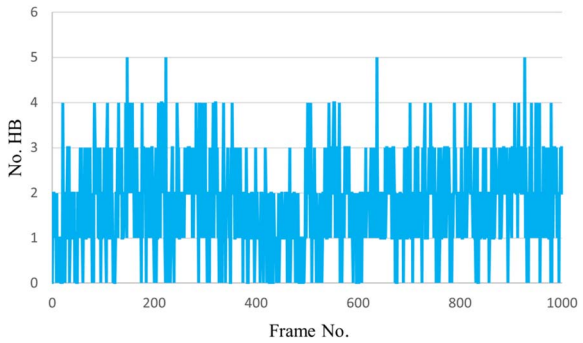

Fig. 17 The H-bonding interactions histogram of protein (**6XHM**) and ligand (**12l**).

three and the maximum is five, which is evident in the strong inhibition of our ligand.

Pharmacokinetic predictions

Pharmacokinetic properties of the most potent derivatives (**12a, 12j, 12k, 12l**) were evaluated using *in silico* tools to predict their potential for Blood–Brain Barrier (BBB) penetration, Human Intestinal Absorption (HIA), and AMES toxicity.

The SMILES strings of these synthesized compounds were submitted to the online admetSAR server (**https://lmmd.ecust.edu.cn/admetsar2/**) for prediction.

As summarized in Table 1, the results indicate that all tested compounds are likely to penetrate the BBB, exhibit significant absorption in the intestine, and are predicted to be non-AMES toxic. These predictions suggest favourable pharmacokinetic

Table 1 Pharmacokinetic properties of the most potent derivatives (**12a**, **12j**, **12k**, **12l**)

Comp. no.	BBB	HIA	AMES toxicity
12a	−(0.9399)	+(0.8739)	Non-toxic (0.5949)
12j	−(0.9205)	+(0.6844)	Non-toxic (0.5488)
12k	−(0.8224)	+(0.5774)	Non-toxic (0.5496)
12l	−(0.9665)	+(0.8197)	Non-toxic (0.6035)

profiles, underscoring their potential for further development as therapeutic agents against SARS-CoV-2 M^{pro}.[81]

Conclusions

The study harnessed the dihydropyrimidine-2-thiones as a scaffold due to its extensive applications in various medications and the availability of an in-house library within our research group. Among diverse derivatized dihydropyridines-2-thiones, **6a**, **6b**, and **6c** DHPM's based intermediate emerged as potent leads subsequently optimized through Structure Activity Relationship (SAR) and computational docking interaction analysis through AutoDock4 version (v4.2.6). These intermediates were also docked and subjected to *in vitro* analysis. Conclusively the study identifies fifteen potent dihydropyrimidine-2-thione-based compounds (**12a–l**) as potential inhibitors of SARS-CoV-2 M^{pro}. These compounds underwent biological assay against the M^{pro} confirming significant inhibitory activity. Notably, compounds (**12a**), **12j**, **12k**, and **12l** exhibited superior inhibition compared to the standard drug **GC376**. Conversely, compounds (**12b**), (**12c**), (**12e**), (**12f**), (**12g**), and (**12i**) demonstrated less inhibitory efficacy. Molecular docking and Molecular Dynamic (MD) simulation revealed significant coherence with biological assay and confirmed the ligand (**12l**)–protein complex (**6XHM**) stability respectively. The cytotoxic profile of compounds **12c**, **12i**, **12j**, **12k**, and **12l** were evaluated, with CC_{50} values confirming an acceptable safety margin for human consumption. Furthermore, the oral toxicity of compounds **12j**, and **12l** were predicted and these were found inactive to the oral toxicities. Collectively designating these compounds as promising non-covalent inhibitors for M^{pro}, compound **12l** exhibited exceptional potency against the M^{pro} of SARS-CoV-2.

Data availability

The data supporting this article have been included as part of the ESI.†

Author contributions

Umer Rashid conceived, designed, and supervised this study. He was involved in all the phases (from synthesis to pharmacological evaluation and manuscript writing/editing) that led to the manuscript's completion. Anees Saeed synthesized the compounds. *In vitro* experiments were performed by Anees Saeed, Fahad Hussain, and Abdul Sadiq. Docking studies were performed by Anees Saeed. Docking results were analyzed and written by Ayesha Tahir and UR. MD simulations were performed by Muhammad Shah. The manuscript was drafted by Anees Saeed. Umer Rashid reviewed and edited the drafts. All the authors have read the manuscript and approved it for publication.

Conflicts of interest

The authors declare no conflict of interest.

Acknowledgements

The research is financially supported by a Project Grant from the Higher Education Commission Pakistan to Umer Rashid (PI) under the National Research Program for Universities (NRPU) (20-14513/NRPU/R&D/HEC/2021 2021).

References

1 A. R. Fehr and S. Perlman, *Coronaviruses: Methods and Protocols*, 2015, pp. 1–23.
2 W. S. T. Consortium, *N. Engl. J. Med.*, 2021, **384**, 497–511.
3 L. Riva, S. Yuan, X. Yin, L. Martin-Sancho, N. Matsunaga, L. Pache, S. Burgstaller-Muehlbacher, P. D. De Jesus, P. Teriete and M. V. Hull, *Nature*, 2020, **586**, 113–119.
4 D. R. Owen, C. M. Allerton, A. S. Anderson, L. Aschenbrenner, M. Avery, S. Berritt, B. Boras, R. D. Cardin, A. Carlo and K. J. Coffman, *Science*, 2021, **374**, 1586–1593.
5 P. V'kovski, A. Kratzel, S. Steiner, H. Stalder and V. Thiel, *Nat. Rev. Microbiol.*, 2021, **19**, 155–170.
6 M. M. Lamers and B. L. Haagmans, *Nat. Rev. Microbiol.*, 2022, **20**, 270–284.
7 D. Cucinotta and M. Vanelli, *Acta Bio Med. Atenei Parmensis*, 2020, **91**, 157.
8 E. Mahase, *BMJ*, 2020, **368**, m1036.
9 D. S. Hui, E. I. Azhar, T. A. Madani, F. Ntoumi, R. Kock, O. Dar, G. Ippolito, T. D. Mchugh, Z. A. Memish and C. Drosten, *Int. J. Infect. Dis.*, 2020, **91**, 264–266.
10 F. G. Hayden, R. B. Turner, J. M. Gwaltney, K. Chi-Burris, M. Gersten, P. Hsyu, A. K. Patick, G. J. Smith III and L. S. Zalman, *Antimicrob. Agents Chemother.*, 2003, **47**, 3907–3916.
11 Y. Kim, H. Liu, A. C. Galasiti Kankanamalage, S. Weerasekara, D. H. Hua, W. C. Groutas, K.-O. Chang and N. C. Pedersen, *PLoS Biol.*, 2016, **12**, e1005531.
12 H. Yang, W. Xie, X. Xue, K. Yang, J. Ma, W. Liang, Q. Zhao, Z. Zhou, D. Pei and J. Ziebuhr, *PLoS Biol.*, 2005, **3**, e324.
13 W. Dai, B. Zhang, X.-M. Jiang, H. Su, J. Li, Y. Zhao, X. Xie, Z. Jin, J. Peng and F. Liu, *Science*, 2020, **368**, 1331–1335.
14 Y. Chen, Q. Liu and D. Guo, *J. Med. Virol.*, 2020, **92**, 418–423.
15 S. Hussain, J. a. Pan, Y. Chen, Y. Yang, J. Xu, Y. Peng, Y. Wu, Z. Li, Y. Zhu and P. Tien, *J. Virol.*, 2005, **79**, 5288–5295.
16 R. Ramajayam, K.-P. Tan and P.-H. Liang, *Biochem. Soc. Trans.*, 2011, **39**, 1371–1375.
17 K. Anand, G. J. Palm, J. R. Mesters, S. G. Siddell, J. Ziebuhr and R. Hilgenfeld, *EMBO J.*, 2002, **21**, 3213–3224.
18 H. Yang, M. Yang, Y. Ding, Y. Liu, Z. Lou, Z. Zhou, L. Sun, L. Mo, S. Ye and H. Pang, *Proc. Natl. Acad. Sci. U. S. A.*, 2003, **100**, 13190–13195.
19 S. Zhang, M. Krumberger, M. A. Morris, C. M. T. Parrocha, A. G. Kreutzer and J. S. Nowick, *Eur. J. Med. Chem.*, 2021, **218**, 113390.
20 K. Świderek and V. Moliner, *Chem. Sci.*, 2020, **11**, 10626–10630.
21 M. Bartlam, H. Yang and Z. Rao, *Curr. Opin. Struct. Biol.*, 2005, **15**, 664–672.

22 D. Stern and B. Sefton, *J. Virol.*, 1982, **44**, 804–812.
23 M. A. Marra, S. J. Jones, C. R. Astell, R. A. Holt, A. Brooks-Wilson, Y. S. Butterfield, J. Khattra, J. K. Asano, S. A. Barber and S. Y. Chan, *Science*, 2003, **300**, 1399–1404.
24 D. F. Veber, S. R. Johnson, H.-Y. Cheng, B. R. Smith, K. W. Ward and K. D. Kopple, *J. Med. Chem.*, 2002, **45**, 2615–2623.
25 R. L. Hoffman, R. S. Kania, M. A. Brothers, J. F. Davies, R. A. Ferre, K. S. Gajiwala, M. He, R. J. Hogan, K. Kozminski and L. Y. Li, *J. Med. Chem.*, 2020, **63**, 12725–12747.
26 Y. Unoh, S. Uehara, K. Nakahara, H. Nobori, Y. Yamatsu, S. Yamamoto, Y. Maruyama, Y. Taoda, K. Kasamatsu and T. Suto, *J. Med. Chem.*, 2022, **65**, 6499–6512.
27 J. D. Tyndall, *J. Med. Chem.*, 2022, **65**, 6496–6498.
28 S. G. V. Rosa and W. C. Santos, *Rev. Panam. Salud Públic*, 2020, **44**, e40.
29 N. Drayman, J. K. DeMarco, K. A. Jones, S.-A. Azizi, H. M. Froggatt, K. Tan, N. I. Maltseva, S. Chen, V. Nicolaescu and S. Dvorkin, *Science*, 2021, **373**, 931–936.
30 Z. Jin, X. Du, Y. Xu, Y. Deng, M. Liu, Y. Zhao, B. Zhang, X. Li, L. Zhang and C. Peng, *Nature*, 2020, **582**, 289–293.
31 C. Ma, M. D. Sacco, B. Hurst, J. A. Townsend, Y. Hu, T. Szeto, X. Zhang, B. Tarbet, M. T. Marty and Y. Chen, *Cell Res.*, 2020, **30**, 678–692.
32 L. Fu, F. Ye, Y. Feng, F. Yu, Q. Wang, Y. Wu, C. Zhao, H. Sun, B. Huang and P. Niu, *Nat. Commun.*, 2020, **11**, 1–8.
33 P. Aparoy, K. Kumar Reddy and P. Reddanna, *Curr. Med. Chem.*, 2012, **19**, 3763–3778.
34 A. Saeed, S. A. Ejaz, A. Khalid, P. A. Channar, M. Aziz, Q. Abbas, T. A. Wani, N. A. Alsaif, M. M. Alanazi and A. M. Al-Hossaini, *Int. J. Mol. Sci.*, 2022, **23**, 13164.
35 A. Elmaghraby, I. Mousa, A. Harb and M. Mahgoub, *Int. Scholarly Res. Not.*, 2013, **2013**, 706437.
36 F. Sánchez-Sancho, M. Escolano, D. Gaviña, A. G. Csáky, M. Sánchez-Roselló, S. Díaz-Oltra and C. Del Pozo, *Pharmaceuticals*, 2022, **15**, 948.
37 I. S. Zorkun, S. Saraç, S. Çelebi and K. Erol, *Bioorg. Med. Chem.*, 2006, **14**, 8582–8589.
38 R. Kaur, S. Chaudhary, K. Kumar, M. K. Gupta and R. K. Rawal, *Eur. J. Med. Chem.*, 2017, **132**, 108–134.
39 G. C. Rovnyak, K. S. Atwal, A. Hedberg, S. D. Kimball, S. Moreland, J. Z. Gougoutas, B. C. O'Reilly, J. Schwartz and M. F. Malley, *J. Med. Chem.*, 1992, **35**, 3254–3263.
40 S. M. D. Rizvi, S. Shakil and M. Haneef, *EXCLI Journal*, 2013, **12**, 831.
41 R. Quiroga and M. A. Villarreal, *PLoS One*, 2016, **11**, e0155183.
42 A. A. Jabbar, R. A. Mothana, M. A. Abdulla, F. O. Abdullah, K. A.-A. Ahmed, R. R. Hussen, M. F. Hawwal, O. I. Fantoukh and S. Hasson, *Saudi Pharm. J.*, 2023, **31**, 101850.
43 M. A. Abu-Zaied, G. H. Elgemeie and N. M. Mahmoud, *ACS Omega*, 2021, **6**, 16890–16904.
44 N. P. Marques, C. S. Lopes, N. C. T. Marques, L. Cosme-Silva, T. M. Oliveira, C. Duque, V. T. Sakai and J. A. C. Hanemann, *Laser Med. Sci.*, 2019, **34**, 465–471.
45 C. Shivanika, D. Kumar, V. Ragunathan, P. Tiwari and A. Sumitha, *J. Biomol. Struct. Dyn.*, 2022, **40**, 585–611.
46 E. Radchenko, A. Dyabina, V. Palyulin and N. Zefirov, *Russ. Chem. Bull.*, 2016, **65**, 576–580.
47 B. H. Sarvaiya, P. I. Vaja, N. A. Paghdar and S. M. Ghelani, *J. Heterocycl. Chem.*, 2024, **61**, 1325–1348.
48 Z. Wang, H. Zhang, Z. Gao, Z. Sang, E. De Clercq, C. Pannecouque, D. Kang, P. Zhan and X. Liu, *Acta Pharm. Sin. B*, 2024, **14**, 1257–1282.
49 C. Gege, F. Hahn, C. Wangen, S. Häge, A. Herrmann, N. Uhlig, V. Eberlein, L. Issmail, R. Klopfleisch and T. Grunwald, *ChemMedChem*, 2024, e202400292.
50 A. M. Elshamsy, T. F. Ali, M. Osman and N. A. El-Koussi, *Journal of Advanced Biomedical and Pharmaceutical Sciences*, 2023, **6**, 114–123.
51 D. S. E. Sayed and E.-S. M. Abdelrehim, *BMC Chem.*, 2022, **16**, 82.
52 D. C. Schultz, R. M. Johnson, K. Ayyanathan, J. Miller, K. Whig, B. Kamalia, M. Dittmar, S. Weston, H. L. Hammond and C. Dillen, *Nature*, 2022, **604**, 134–140.
53 E. Mansour, A. M. Sayed and S. I. Elewa, *Polycyclic Aromat. Compd.*, 2024, 1–26.
54 R. Xiong, L. Zhang, S. Li, Y. Sun, M. Ding, Y. Wang, Y. Zhao, Y. Wu, W. Shang and X. Jiang, *Protein Cell*, 2020, **11**, 723–739.
55 U. Rashid, S. F. Hassan, S. Nazir, A. Wadood, M. Waseem and F. L. Ansari, *Med. Chem. Res.*, 2015, **24**, 304–315.
56 U. Rashid, R. Sultana, N. Shaheen, S. F. Hassan, F. Yaqoob, M. J. Ahmad, F. Iftikhar, N. Sultana, S. Asghar and M. Yasinzai, *Eur. J. Med. Chem.*, 2016, **115**, 230–244.
57 G. Ahmad, N. Rasool, K. Rizwan, A. A. Altaf, U. Rashid, M. Z. Hussein, T. Mahmood and K. Ayub, *Molecules*, 2019, **24**, 2609.
58 M. J. Ahmad, S. F. Hassan, R. U. Nisa, K. Ayub, M. S. Nadeem, S. Nazir, F. L. Ansari, N. A. Qureshi and U. Rashid, *Med. Chem. Res.*, 2016, **25**, 1877–1894.
59 F. Iftikhar, F. Yaqoob, N. Tabassum, M. S. Jan, A. Sadiq, S. Tahir, T. Batool, B. Niaz, F. L. Ansari and M. I. Choudhary, *Bioorg. Chem.*, 2018, **80**, 99–111.
60 M. Bibi, N. A. Qureshi, A. Sadiq, U. Farooq, A. Hassan, N. Shaheen, I. Asghar, D. Umer, A. Ullah and F. A. Khan, *Eur. J. Med. Chem.*, 2021, **210**, 112986.
61 M. A. Javed, N. Ashraf, M. Saeed Jan, M. H. Mahnashi, Y. S. Alqahtani, B. A. Alyami, A. O. Alqarni, Y. I. Asiri, M. Ikram and A. Sadiq, *ACS Chem. Neurosci.*, 2021, **12**, 4123–4143.
62 L. Zhang, D. Lin, X. Sun, U. Curth, C. Drosten, L. Sauerhering, S. Becker, K. Rox and R. Hilgenfeld, *Science*, 2020, **368**, 409–412.
63 C.-H. Zhang, E. A. Stone, M. Deshmukh, J. A. Ippolito, M. M. Ghahremanpour, J. Tirado-Rives, K. A. Spasov, S. Zhang, Y. Takeo and S. N. Kudalkar, *ACS Cent. Sci.*, 2021, **7**, 467–475.
64 A. Thakur, G. Sharma, V. N. Badavath, V. Jayaprakash, K. M. Merz Jr, G. Blum and O. Acevedo, *J. Phys. Chem. Lett.*, 2022, **13**, 5776–5786.
65 S. Tomar, M. L. Johnston, S. E. S. John, H. L. Osswald, P. R. Nyalapatla, L. N. Paul, A. K. Ghosh, M. R. Denison and A. D. Mesecar, *J. Biol. Chem.*, 2015, **290**, 19403–19422.

66 J. Mondal, P. Tiwary and B. Berne, *J. Am. Chem. Soc.*, 2016, **138**, 4608–4615.
67 H. H. Chan, M. A. Moesser, R. K. Walters, T. R. Malla, R. M. Twidale, T. John, H. M. Deeks, T. Johnston-Wood, V. Mikhailov and R. B. Sessions, *Chem. Sci.*, 2021, **12**, 13686–13703.
68 C. Zhang, *ACS omega*, 2022, **7**, 18206–18212.
69 C. Ma, Y. Hu, J. A. Townsend, P. I. Lagarias, M. T. Marty, A. Kolocouris and J. Wang, *ACS Pharmacol. Transl. Sci.*, 2020, **3**, 1265–1277.
70 W. Vuong, M. B. Khan, C. Fischer, E. Arutyunova, T. Lamer, J. Shields, H. A. Saffran, R. T. McKay, M. J. van Belkum and M. A. Joyce, *Nat. Commun.*, 2020, **11**, 4282.
71 A. K. Ghosh, M. Brindisi, D. Shahabi, M. E. Chapman and A. D. Mesecar, *ChemMedChem*, 2020, **15**, 907–932.
72 I. Y. Akbayrak, S. I. Caglayan, L. Kurgan, V. N. Uversky and O. Coskuner-Weber, *Curr. Res. Struct. Biol.*, 2022, **4**, 349–355.
73 A. Chandra Manivannan, A. Malaisamy, M. Eswaran, A. Meyyazhagan, V. A. Arumugam, K. R. Rengasamy, B. Balasubramanian and W.-C. Liu, *Front. Mol. Biosci.*, 2022, **9**, 918101.
74 A. M. Shaqra, S. N. Zvornicanin, Q. Y. J. Huang, G. J. Lockbaum, M. Knapp, L. Tandeske, D. T. Bakan, J. Flynn, D. N. Bolon and S. Moquin, *Nat. Commun.*, 2022, **13**, 3556.
75 M. Macchiagodena, M. Pagliai and P. Procacci, *Chem. Phys. Lett.*, 2020, **750**, 137489.
76 C. Lin, H. Jiang, W. Li, P. Zeng, X. Zhou, J. Zhang and J. Li, *Structure*, 2023, **31**, 1016–1024.e3.
77 H. P. Shao, T. H. Wang, H. L. Zhai, K. X. Bi and B. Q. Zhao, *Chem.-Biol. Interact.*, 2023, **371**, 110352.
78 L. Alzyoud, M. A. Ghattas and N. Atatreh, *Drug Des., Dev. Ther.*, 2022, **16**, 2463.
79 Q. Hu, Y. Xiong, G. H. Zhu, Y. N. Zhang, Y. W. Zhang, P. Huang and G. B. Ge, *MedComm*, 2022, **3**, e151.
80 M. D. Sacco, C. Ma, P. Lagarias, A. Gao, J. A. Townsend, X. Meng, P. Dube, X. Zhang, Y. Hu and N. Kitamura, *Sci. Adv.*, 2020, **6**, eabe0751.
81 J. Shen, F. Cheng, Y. Xu, W. Li and Y. Tang, *J. Chem. Inf. Model.*, 2010, **50**, 1034–1041.